Ductile fracture of high entropy alloys: from the design of an experimental campaign to the development of a micromechanics-based modeling framework

Antoine Hilhorst[b], Julien Leclerc[a], Thomas Pardoen[b], Pascal J. Jacques[b], Ludovic Noels[a,*], Van-Dung Nguyen[a,1]

[a]*Computational & Multiscale Mechanics of Materials, Department of Aerospace and Mechanical Engineering, University of Liège, B-4000 Liège, Belgium*
[b]*UCLouvain, Institute of Mechanics, Materials and Civil Engineering (iMMC), IMAP, Place Sainte Barbe 2, Université catholique de Louvain, Louvain-la-Neuve 1348, Belgium*

Abstract

Cantor-type high entropy alloys form a new family of metallic alloys characterised by a combination of high strength and high fracture toughness. An experimental study on the CoCrNi alloy is first performed to determine the damage and fracture mechanisms under various stress states. A micromechanics-based ductile fracture model is identified and validated using these experimental data. The model corresponds to a hyperelastic finite strain multi-yield surface constitutive description coupled with multiple nonlocal variables. The yield surfaces consist of three distinct nonlocal solutions corresponding to three different modes of void expansion within an elastoplastic matrix: a void growth mode governed by a Gurson-based yield surface corrected for shear effects, an internal necking-driven coalescence mode governed by an extension of the Thomason yield surface based on the maximum principal stress, and a shear-driven coalescence mode governed by the maximum shear stress. This advanced formulation embedded in large strain finite element setup captures the effects not only of the stress triaxiality but also of the Lode variable. In particular, the analysis shows that a failure model accounting for these two invariants of the stress tensor captures the fracture in high-entropy alloys over a wide range of conditions.

Keywords: Ductile Fracture, High Entropy Alloy, Constitutive model, Experiment

1. Introduction

In recent years, complex concentrated alloys, better known as High Entropy Alloys (HEAs), consisting of multi-principal element alloys with typically 3 to 5 elements in equal or near equiatomic concentrations,

---

*Corresponding author, Phone: +32 4 366 48 26, Fax: +32 4 366 95 05
Email address: `L.Noels@ulg.ac.be` (Ludovic Noels)
[1]Postdoctoral Researcher at the Belgian National Fund for Scientific Research (FNRS)

garnered a lot of attention [1, 2, 3]. This novel alloy design philosophy gave rise to several alloy systems with interesting combinations of mechanical (and functional) properties. Among HEAs, Cantor-based alloys (the Co-Cr-Fe-Mn-Ni system) constitute a promising family of alloys characterised by a combination of high strength, high ductility, and high fracture toughness [4, 5, 6]. The excellent mechanical properties of the Cantor-based HEAs are often attributed to deformation twinning [7, 8]. As such, constitutive modeling of HEAs focuses in large part on the evolution of dislocations and twins with strain [9, 10]. Recently, it was shown that the ternary CoCrNi alloy presents exceptional levels of fracture resistance [6, 11, 12].

Attempts to understand and model ductile fracture in the context of micromechanics approaches in HEAs are scarce. Gao et al. [13] characterized the damage and fracture in the CoCrFeNiMo HEA under multi-axial stress states but the behavior was not modeled. Lu et al. [14] addressed the damage evolution in the CoCrFeNi alloy. Different stress states were considered, however the emphasis was on the texture and strain rate effects. Cui et al. [15] modeled the fracture of CoCrFeMnNi films through an atomistic study. The results were not compared to experiments. The integrated design of an experimental campaign, identification of an adequate failure micro-mechanical modeling and characterization is still missing in the context of HEAs.

Ductile fracture is the most common failure mode for most metals and their alloys, see *e.g.* [16, 17, 18]. Ductile fracture involves a damage mechanism related to the evolution of micro-voids, consisting of three successive stages involving the nucleation, growth and coalescence associated to extensive plastic deformation before final failure. Micro-voids generally nucleate from either particle fracture or particle decohesion [19]. Under macroscopic loading conditions, the nucleated voids and the existing ones, which may pre-exist from manufacturing, grow and change their shape through plastic deformation. This growth stage is interrupted by localization of the plastic flow in the ligament between the voids, which corresponds to the onset of void coalescence. Finally, the voids coalesce, resulting in macroscopic cracking initiation and propagation. We will show in this work that the failure of the investigated HEAs follows these usual stages and can thus be adequately captured by a micromechanics-based ductile fracture model.

The most popular micromechanics-based ductile failure model is the Gurson model [20], in which fracture is taken into account in a physically motivated way through evolution of porosity in metals. The original model was further extended in order to account for void nucleation, void growth, void coalescence, void shape, void distribution, plastic anisotropy, shear effects, *etc.* [21, 22, 23, 24, 25, 26, 27, 28, 29, 30, 31]. In particular, the Gurson–Tvergaard–Needleman (GTN) model [21, 22] in combination with a shear enhanced term suggested by Nahshon and Hutchinson [30] to better capture the porosity effect on the constitutive response under low stress triaxiality is extensively applied to large-scale structural modeling due to its numerical simplicity. Although this enhanced GTN model provides a complete computational methodology for all stages of void evolution, its description of void coalescence is not realistic as it relies on an abrupt void growth rate beyond a critical value of the porosity [32]. Indeed, as observed in the finite element unit cell

simulations [33, 32], at the onset of coalescence by internal necking, the material behavior suddenly changes into a localised deformation state, indicating a transition to another mode of plastic flow around the voids. In this context, micromechanics-based coalescence models as pioneered by [34, 35] provide a better physical description, in which the coalescence occurs when the plastic flow localises inside the inter-void ligament oriented normal to the main loading direction. This so-called Thomason model was further extended to better represent the internal necking coalescence process [32, 36, 37, 38]. However, the Thomason model and its extended forms do not account for possibly shear-dominated coalescence primarily observed at low stress triaxiality. To address this issue, micromechanical-based conditions for the onset of void coalescence under combined tension and shear were proposed [39, 40].

Recently, both internal necking void coalescence and shear-driven coalescence were accounted for in a single micromechanics-based model by introducing a porous plasticity incorporating multiple yield surfaces [41]. This model considers the three distinct solutions for the expansion of voids embedded in an elastoplastic matrix: a void growth solution governed by the GTN yield surface, a void necking coalescence solution driven by the maximum principal stress corresponding to an extension of the Thomason yield surface, and a competing void shearing coalescence solution driven by the maximum shear stress. This combination allows capturing the effects not only of the Lode variable characterising among others shear effects, but also the stress triaxiality in ductile fracture process in which case these two parameters play important roles. In order to avoid loss of solution uniqueness beyond the onset of material softening, this multi-surface model was framed in an implicit nonlocal form [42, 43] through the introduction of multiple nonlocal variables governing the different failure mechanisms of the model. We will show here that this multi-yield surface multi-nonlocal variable micromechanics-based ductile failure model is a good candidate to represent the failure of highly ductile HEAs.

The first objective of this work is the determination of the physical damage mechanisms in the novel damage-resistant CoCrNi alloy through experimental analyses by designing an experimental campaign covering different stress-states. Macro-scale stress-strain responses as well as micro-structural observations such as porosity evolution are extracted from different test specimens. This extensive experimental study confirms that the failure of CoCrNi HEA follows the expected ductile mechanisms involving the different described stages of void evolution: void nucleation by matrix-inclusion decohesion, void growth, shear localization and internal necking fracture modes. The stress triaxiality and Lode variable are also shown to strongly affect the fracture behavior. The Lode variable strongly affects the fracture mode and the fracture surface morphology. These observations justify considering the multi-yield surface multi-nonlocal variable micromechanics-based ductile failure model [41] to model the failure of these complex fracture behaviors involving shear localization and internal necking fracture mechanisms. The second aim of this work is thus to develop an efficient strategy for the identification of the model material parameters. These identified parameters values are then validated, showing good predictive capability over a wide range of stress states.

The paper is organised as follows. Section 2 describes the experiment campaign. The micromechanics-based model developed in the work [41] is recalled in Section 3. Finally, the identification of the material parameters as well as the validation are presented in Section 4.

2. Experimental characterization

The material processing of CoCrNi alloy is presented, followed by the experimental mechanical test campaign for the identification of the physical damage mechanisms in the CoCrNi alloy under different loading scenarios. The macro-scale stress-strain response of different specimen geometries and the corresponding post-mortem micro-scale characterization are finally presented.

2.1. Material processing and characterization

Four 1-kg ingots of CoCrNi were processed by vacuum induction melting from pure elements ($>$ 99.8% purity). All ingots were hot-rolled at 1473 K from an initial thickness of 27 mm down to a thickness of 12 mm in two passes. The material dynamically recrystallised during hot rolling and no further heat treatment was carried out. Fig. 1 shows a representative scanning electron microscope (SEM) micrograph of the microstructure after hot-rolling at low magnification. The microstructure is single phase FCC with an average grain size of 25±14 μm. The inclusions are Cr_2O_3 oxides, as identified by energy dispersive spectroscopy (SEM-EDS). The average inclusion content was measured by image analysis as 0.20±0.07%. The average particle diameter is 2.33 ± 0.37 μm. An example of such inclusions is shown in the inset of Fig. 1. Voids were not observed in the initial microstructure.

Electron Back Scatter Diffraction (EBSD) was performed to characterize the microstructure. The Inverse Pole Figure (IPF) map is given in 2(a) with the pole figure of the {111} direction given in 2(b). The material does not show any particular crystallographic texture. A few large grains show a color gradient, indicating the presence of dislocations as the result of dynamic recrystallisation. The grain size distribution follows what has already been reported in Fig. 1. While there exist small and large grains, the distribution of grain size is not bimodal, but the variance of the grain size is quite large for the studied material.

2.2. Mechanical tests

Mechanical tests with different specimen geometries were performed to characterise the effect of the stress state on the damage evolution and fracture mode. All specimens were extracted directly from the as-rolled 12-mm plates by electrical discharge machining (EDM). These specimen geometries are sketched in Fig. 3 including:

- Plate specimens involve smooth specimens (referred as "1L"), tapered specimens designed so that the plastic strain and thus the porosity slowly evolves from the fracture surface (referred as "2PL"), and small notched specimens (referred as "2NSx" with x being the notch radius in mm);
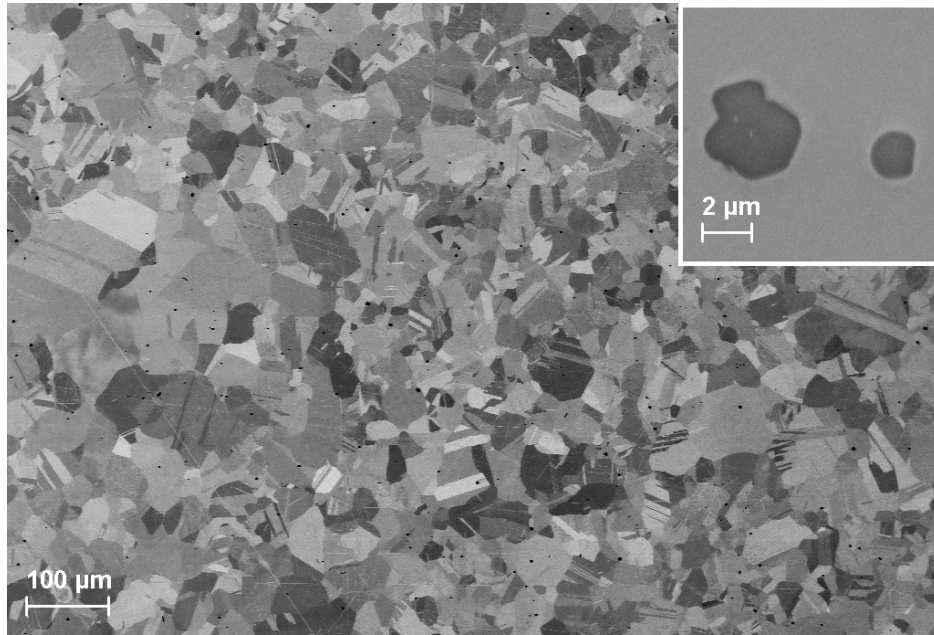
Figure 1: SEM micrograph of the microstructure of CoCrNi after hot-rolling. Inset shows a larger magnification of the type of inclusions present in the alloy.
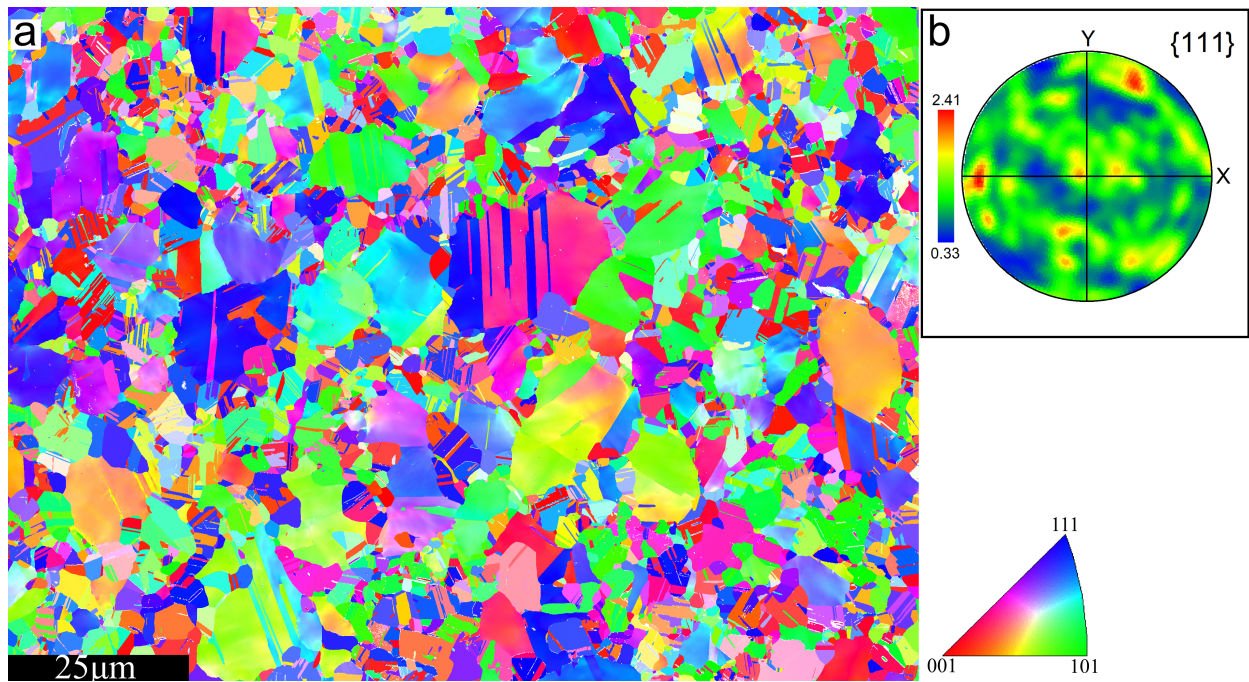

Figure 2: (a) Inverse Pole Figure (IPF) map of the microstructure of CoCrNi and (b) the corresponding pole figure of the {111} direction where X and Y are the longitudinal and transverse direction respective to the rolling direction, respectively.

- Shear specimen (referred as "3SHEAR") with a design inspired from [44];

- Axisymmetric specimens involve smooth specimens (referred as "4SR") and notched specimens (referred as "5NRx" where x is the notch radius);

- Plane strain-type grooved specimens (referred as "7GRx", with x being the groove radius in mm).

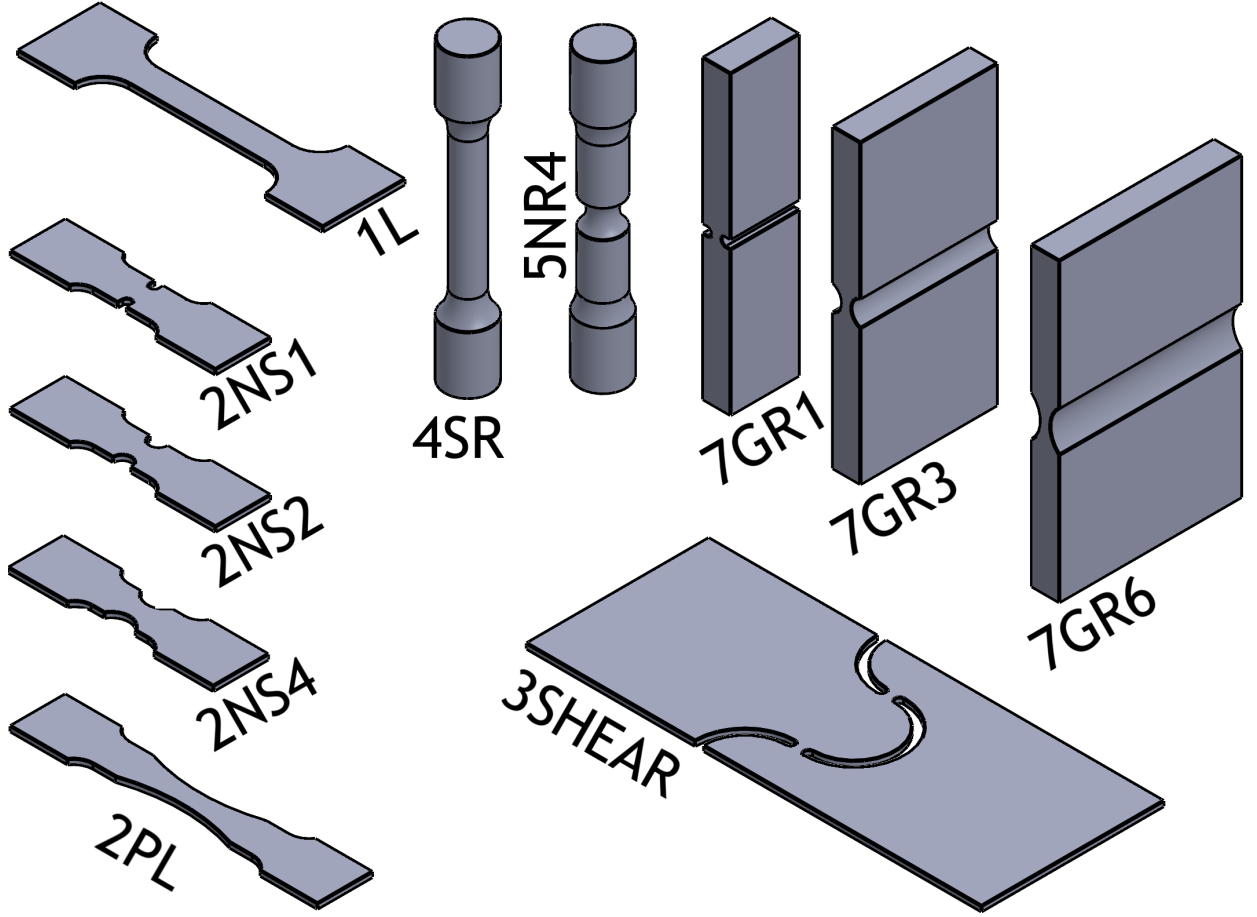The detailed dimensions of the specimens are reported in Appendix A.

Figure 3: Drawings of the plate (1L, 2PL, 2NS, 3SHEAR), axisymmetric (4SR, 5NR), and grooved (7GR) specimens.

These specimens undergo different stress states, which can be characterised by the magnitude of the stress triaxiality (denoted by η) and of the Lode variable (denoted by ω). With the Cauchy stress tensor denoted by $\mathbf{\Sigma}$, these two quantities are estimated as

$$\eta = \frac{\operatorname{tr}(\mathbf{\Sigma})}{3\Sigma_{\text{eq}}} \text{ and } \omega = \frac{27 \det(\operatorname{dev}(\mathbf{\Sigma}))}{2\Sigma_{\text{eq}}^3}, \tag{1}$$

where $\operatorname{tr}(\bullet)$ and $\operatorname{dev}(\bullet)$ are respectively the trace and deviatoric operators, and $\Sigma_{\text{eq}} = \sqrt{\dfrac{3}{2}\operatorname{dev}(\mathbf{\Sigma}) : \operatorname{dev}(\mathbf{\Sigma})}$

6

Table 1: Summary of the specimen geometries used to characterise the material behavior under different stress states.

Family	Description	Abbreviation	γ	η-range*	ω-range*	Gauge length
Plate specimens	Smooth	1L	0	$> 1/3$	(0 1)	25 mm
	Notched	2PL	0.05	$> 1/3$	(0 1)	30 mm
	Notched	2NS4	0.5	$> 1/3$	(0 1)	11 mm
	Notched	2NS2	1	$> 1/3$	(0 1)	11 mm
	Notched	2NS1	2	$> 1/3$	(0 1)	11 mm
Shear specimens	Shear	3SHEAR	0	≈ 0	≈ 0	50 mm
Axisymmetric specimens	Smooth	4SR	0	$> 1/3$	1	25 mm
	Notched	5NR4	0.625	$> 1/3$	1	25 mm
Grooved specimens	Grooved	7GR6	0.167	$> 1/\sqrt{3}$	0	20 mm
	Grooved	7GR3	0.333	$> 1/\sqrt{3}$	0	20 mm
	Grooved	7GR1	1	$> 1/\sqrt{3}$	0	20 mm

* Stress triaxiality η and Lode parameter ω at the centre of the notched section when fracture occurs.

is the von Mises equivalent stress. The stress triaxiality η characterises the contribution of the hydrostatic stress while the Lode variable ω indicates the loading modes: $\omega = 1$ corresponds to a general axisymmetric tension; $\omega = 0$ corresponds to plane strain and general shear loading; and $\omega = -1$ corresponds to a general axisymmetric compression.

In the specimens shown in Fig. 3, the notches with different radii produce different stress states. The presence of a notch in a specimen is characterised by a shape factor (denoted by γ) given by

$$\gamma = \frac{a_0}{R_n} \, , \tag{2}$$

where R_n is the notch radius, and a_0 is defined depending on the specimen geometry: $a_0 = R_0$ is the radius at the minimum cross section in axisymmetric specimens; $a_0 = W_0/2$ where W_0 is the initial width at the minimum section for the plate specimens; $a_0 = t_0/2$ where t_0 is the thickness at the minimum section of the grooved specimens. Since there is no notch in the 3SHEAR specimen, a shape factor equal to 0 is used. All these geometries and their shape factors are summarised in Tab. 1.

The mechanical tests were all performed with a constant cross-head velocity of 1 mm/min. For each test, several (typically 3 repetitions) specimens were considered to assess the variability in the mechanical response. The tensile tests were recorded during the whole experimental loading. Digital image correlation (DIC) is used to track the elongation ΔL over an equivalent gauge of initial length L_0 as reported in Tab. 1, from which the engineering strain is determined as $\Delta L/L_0$. Fig. 4 shows the engineering stress-engineering strain curves obtained for all specimens until final fracture[2]. The engineering stress is computed by F/A_0

---

[2]For one of the 7GR1 specimen, the recording failed during the test. The stress-strain behavior of this specimen was then
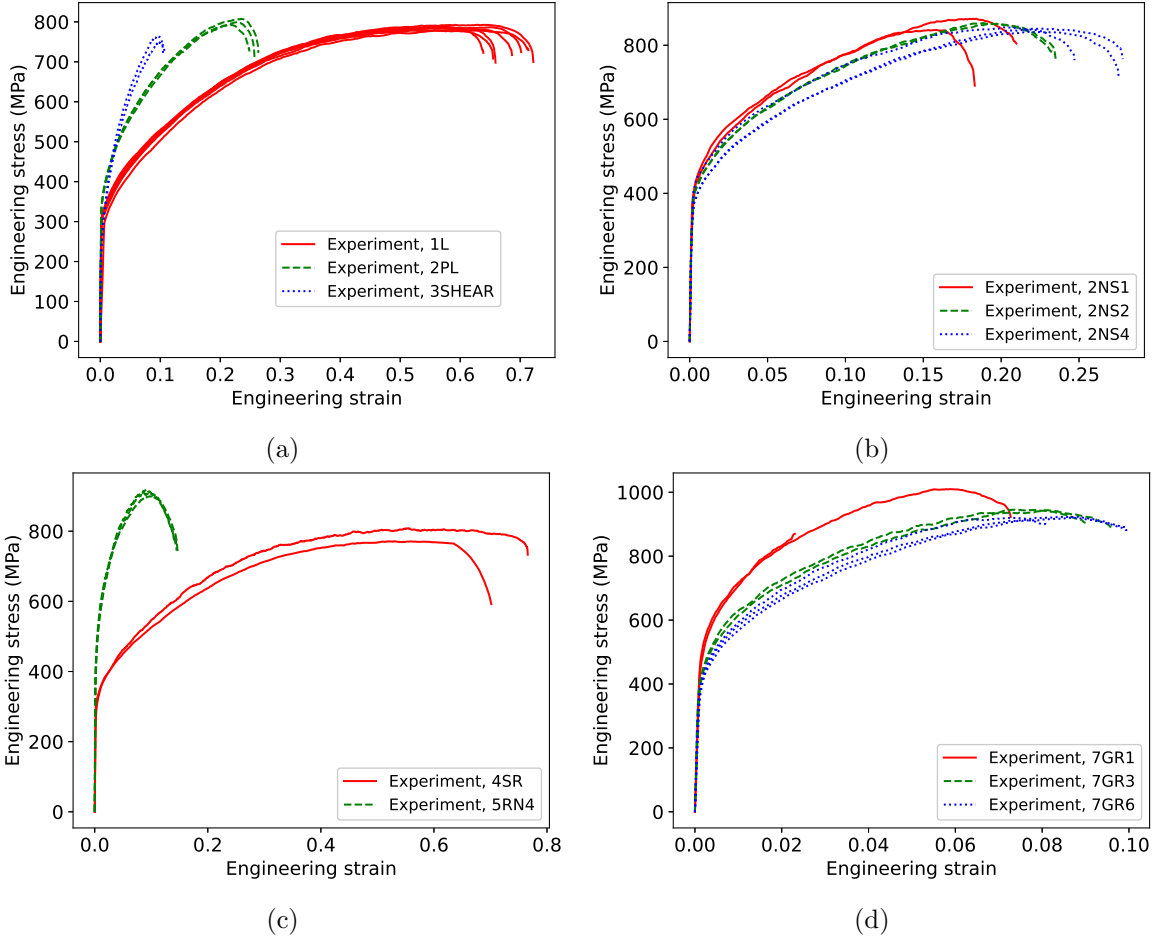
Figure 4: Experimental engineering stress-engineering strain curves: (a) 1L, 2PL and 3SHEAR tests, (b) 2NSx tests, and (c) 4SR and 5NR4 specimens, and (d) 7GRx specimens.

where F is the tensile force and A_0 is the initial area of the minimum cross section. For each specimen type, it can be seen that a smaller notch radius leads to a higher stress level. Smooth specimens (1L and 4SR) can reach a high level of elongation (> 0.6). These curves can be used to estimate the isotropic hardening law over a wide range of plastic deformation when expressed under true stress–true plastic strain format. The 2NSx specimens shows engineering curves close to each other with different notch radius.

The fracture strain is determined for each specimen type [45, 46] as follows:

---

analyzed up to this point, but since the test was performed until fracture, its related fracture strain could be considered as well.

- Plate specimens[3]:

$$\varepsilon_{\text{f}} = \frac{2}{\sqrt{3}} \sqrt{\ln^2 \frac{t_0}{t_f} + \ln^2 \frac{W_0}{W_f} + \ln \frac{t_0}{t_f} \ln \frac{W_0}{W_f}} \,, \tag{3}$$

where W_0 and t_0 are the initial width at the minimum cross section and initial thickness of the specimen and W_f and t_f are the mean values at fracture.

- Axisymmetric specimens:

$$\varepsilon_{\text{f}} = 2 \ln \frac{R_0}{R_f} \,, \tag{4}$$

where R_0 is the initial radius at the minimum cross section and R_f is its corresponding value at fracture.

- Grooved specimens:

$$\varepsilon_{\text{f}} = \frac{2}{\sqrt{3}} \ln \frac{t_0}{t_f} \,, \tag{5}$$

where t_0 is the initial thickness at the minimum cross section and t_f is the corresponding value at fracture.

The fracture strain for all specimens are gathered in Fig. 5 in terms of the shape factor. The HEA exhibits high fracture strain (> 0.85 for all cases). For the 4SR specimens, a fracture strain > 1.2 is reached. In the cases of axisymmetric specimens and grooved specimens, the fracture strain decreases with notch radius due to higher stress triaxiality. The difference among the fracture strains at the same notch radius partly results from the Lode effect, with $\omega = 0$ for the grooved specimens leading to smaller ε_{f} compared to the axisymmetric specimens with $\omega = 1$. Although the stress triaxiality at the notch section increases with decreasing notch radius for these plate specimens, the Lode variable at fracture does not remain constant but varies with the shape factor qualitatively explaining the observed trend, see [46] for more details with a similar specimen type in high strength steel.

---

[3]Based on the assumption that the minimum cross-section at fracture remains rectangular and that, at this stage, deformations are purely deviatoric with a Poisson ratio close to one half, the strain tensor can be approximated as $\boldsymbol{\varepsilon} = \text{diag}\left(\ln \frac{W_0}{W_f}, \ln \frac{t_0}{t_f}, -\ln \frac{W_0}{W_f} - \ln \frac{t_0}{t_f}\right)$. As a result, the equivalent strain definition $\varepsilon_{eq} = \sqrt{\frac{2}{3} \text{dev}(\boldsymbol{\varepsilon}) : \text{dev}(\boldsymbol{\varepsilon})}$ leads to Eq. (3). In addition, Eq. (3) can be directly applied to the axisymmetric specimens with $\boldsymbol{\varepsilon} = \text{diag}\left(\ln \frac{R_0}{R_f}, \ln \frac{R_0}{R_f}, -\ln \frac{R_0}{R_f} - \ln \frac{R_0}{R_f}\right)$, leading to Eq. (4), and to the grooved specimens, with $\boldsymbol{\varepsilon} = \text{diag}\left(\ln \frac{t_0}{t_f}, 0, -\ln \frac{t_0}{t_f}\right)$, leading to Eq. (5).
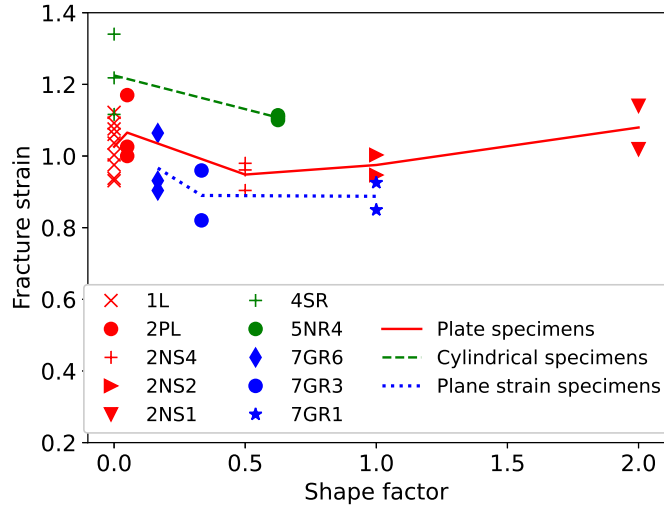
Figure 5: Variation of the fracture strain as a function of the notch shape factor for all test specimens. The data of 3SHEAR are not shown since the macroscopic fracture strain can not be defined in a way consistent with the other geometries.

2.3. Fractographic analysis

Figure 6 shows SEM micrographs of the fracture surfaces of the axisymmetric specimens. The fracture surface consists of a rough part at the centre and a less rough slant part close to the free surface associated to the classical cup–cone morphology. The slant part is inclined at 45° with respect to the loading direction. This corresponds to a fracture driven by shear localization, leading to a different surface appearance compared to the one at the central region in which an internal void coalescence mechanism is observed. The dimple size is quite homogeneous showing that only one population of voids is active.

Figure 7 shows the fracture surface in the 3SHEAR specimen. The fracture mode is controlled by shear localization, in which the fracture surface appearance is similar to the one observed in the slant part of the axisymmetric specimens as reported in Figs. 6.

Figure 8 shows the fracture surfaces of the grooved specimens. The slant fracture mode is observed for the three notch radii. The fracture surface does not consist of sheared and elongated dimples as in Fig. 7 for the 3SHEAR specimen. These dimples are more similar to the one in the tensile specimens. This observation probably relates to the higher stress triaxiality in the grooved specimens which causes more void expansion before void coalescence. The fracture 7GRx specimens occurs at a Lode variable close to zero as it will be confirmed in Section 4.3.2.

Figure 9 shows the fracture surfaces corresponding to the plate specimens: 1L and 2NSx. A slant fracture mode is again observed for all cases. The fracture surface is similar to the cases of the axisymmetric specimens in the slant part, and of the 3SHEAR and 7GRx specimens, and is different to the central part of the fracture surface of the axisymmetric specimens reported in Figs. 6.
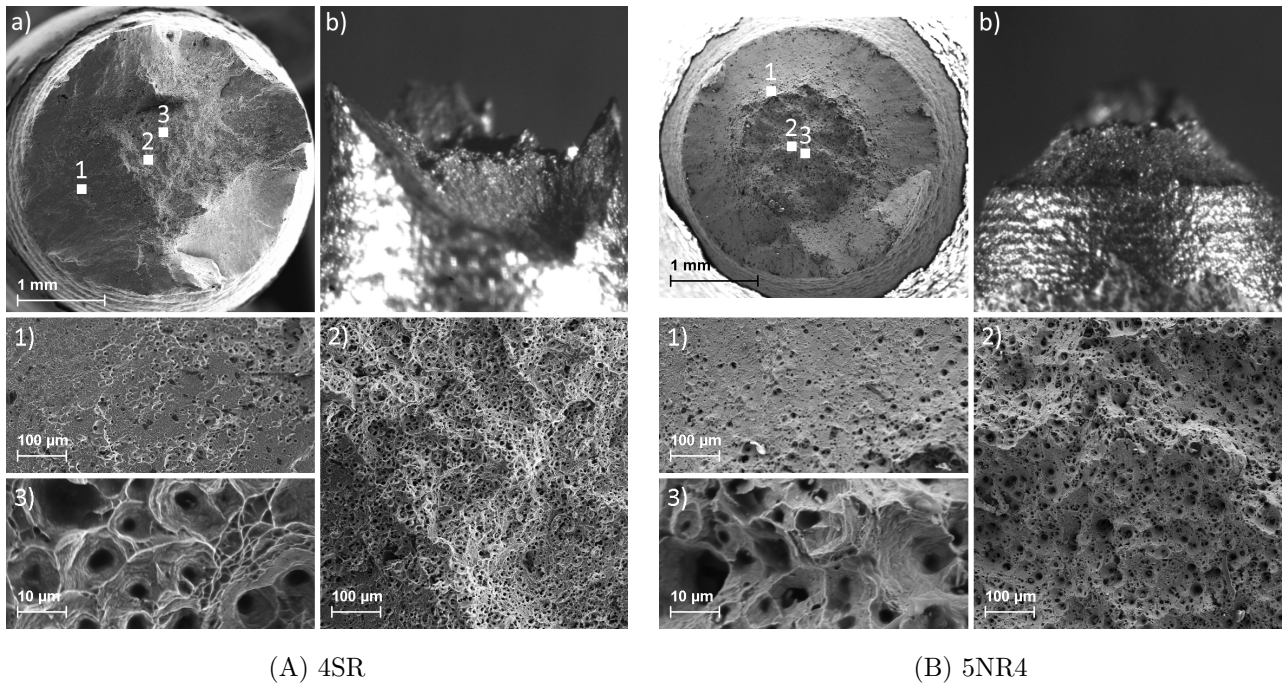
10

Figure 6: Micrographs of the fracture surface of the axisymmetric specimens: (A) 4SR and (B) 5NR4. In each sub-figure, (a) and (b) correspond to the central and side views of the fracture surface, respectively. (1), (2), and (3) provide higher magnification of regions of interest indicated in (a).
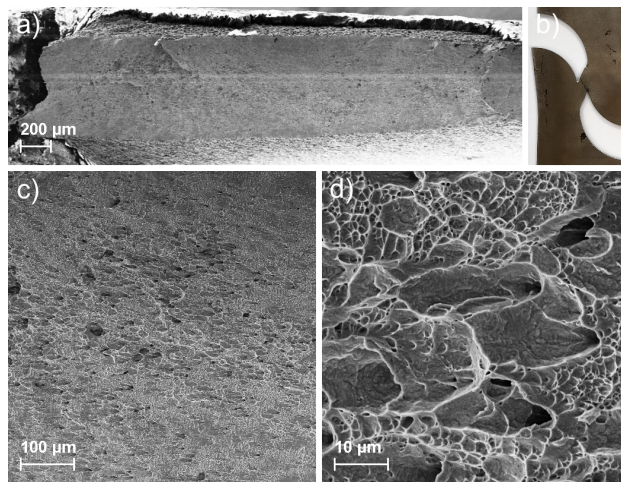

Figure 7: Micrographs of the fracture surface of the 3SHEAR specimens. The top-left figure (a) corresponds to the overall view of the fracture surface and the top-right figure (b) shows the whole fractured specimen. The bottom-left figure (c) and bottom-right figure (d) correspond to higher magnifications of the fracture surface.
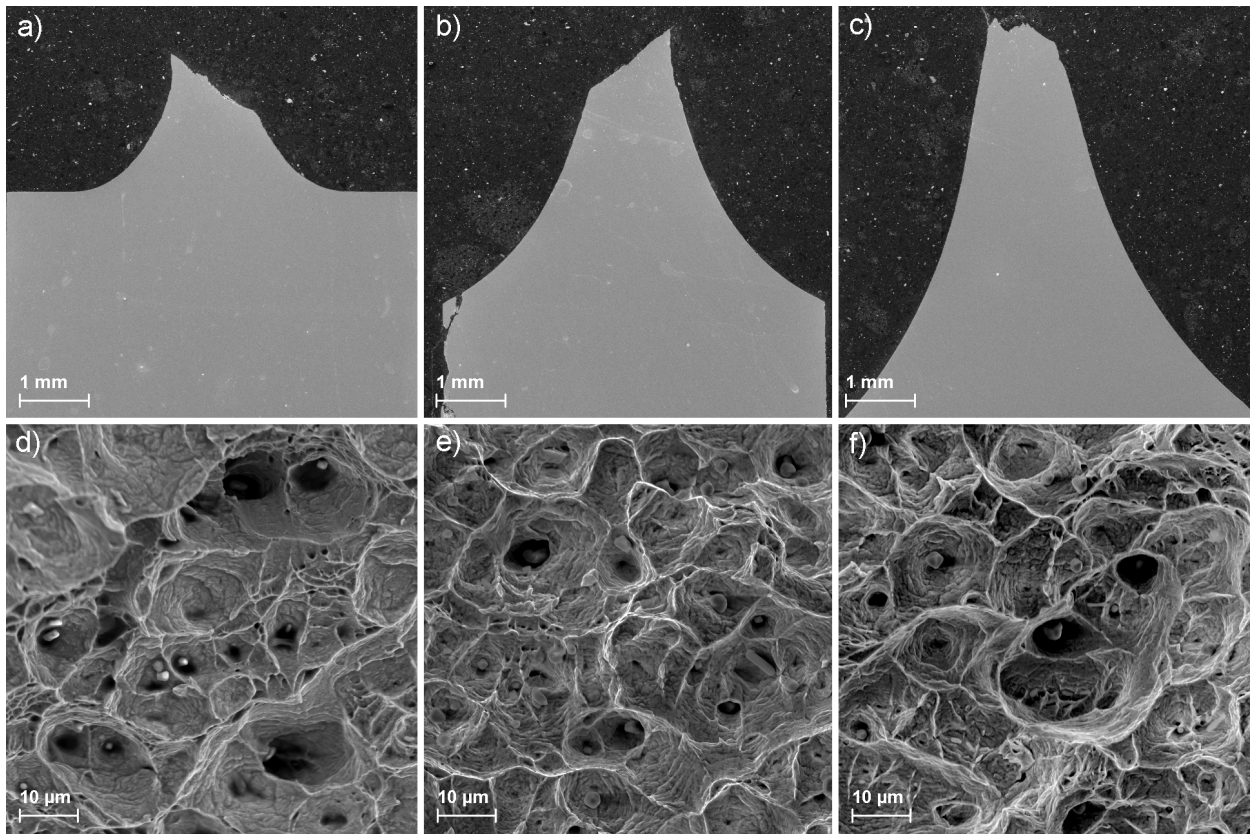
Figure 8: Micrographs of the fracture surface of the 7GRx specimens: left figures (a, d) - 7GR1 specimen, central figures (b, e) - 7GR3 specimen, and right figures (c, f) - 7GR6 specimen. Three top figures correspond to the side views of the fracture surface while the three bottom figures show the corresponding fracture surface at high magnification.
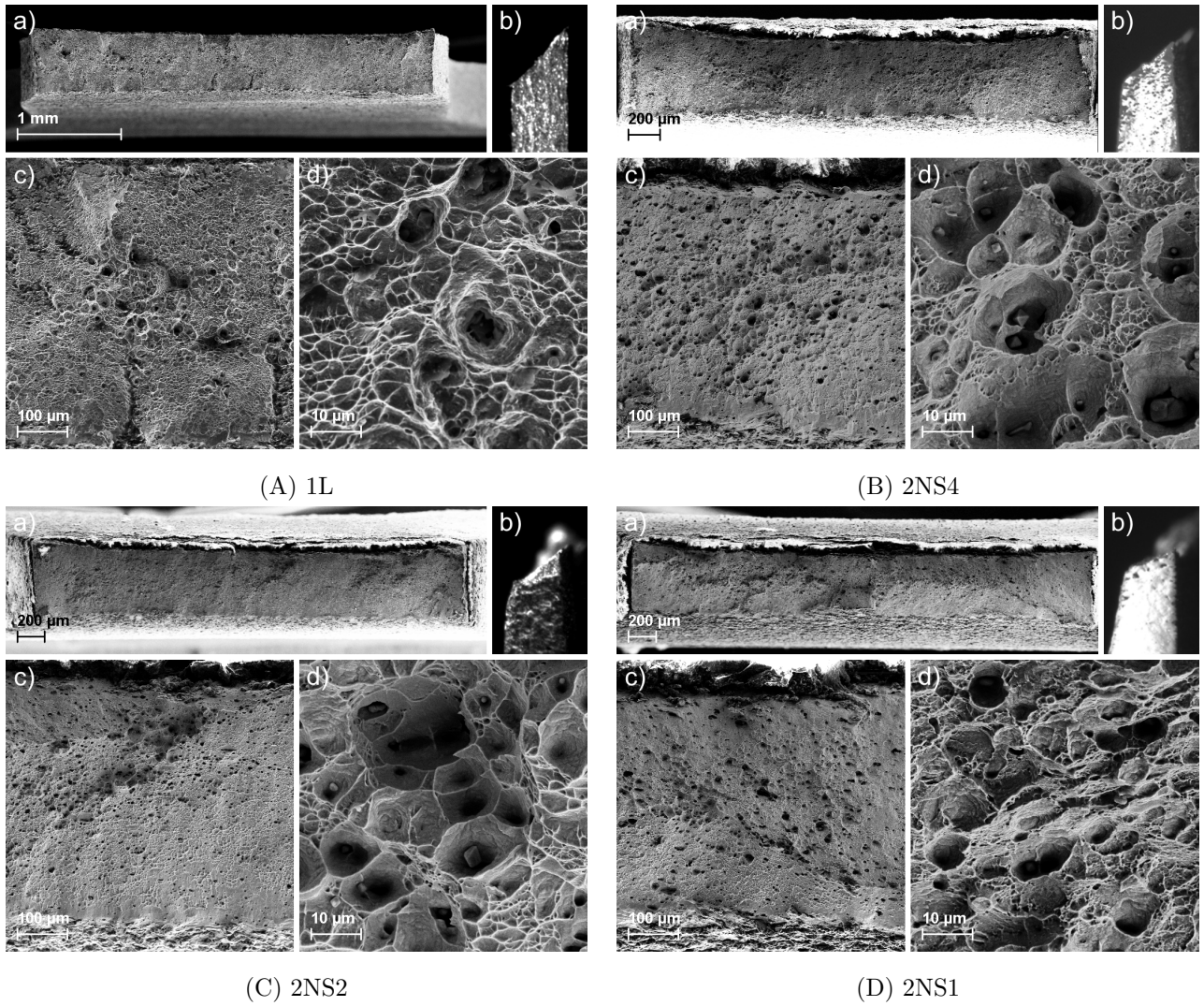
(A) 1L

(B) 2NS4

(C) 2NS2

(D) 2NS1

Figure 9: Micrographs of the fracture surface in the plate specimens. In each sub-figure, the top-left figure (a) corresponds to the overall view of the fracture surface and the top-right figure (b) shows a side-view of the whole fractured specimen. The bottom-left figure (c) and bottom-right figure (d) correspond to the fracture surface at higher magnification.

Figures 6-9 show the present of both larger and smaller voids. In the present CoCrNi alloy, only Cr_2O_3 inclusions are observed. However, there exists a distribution of particles sizes with the smaller particles organized in clusters together with larger isolated particles. This leads to a significant variation of the size of cavities which results not only from the difference in the initial size of the inclusions, but also from the difference in the strain at which the inclusions nucleate (since void nucleation often occurs earlier on larger particles[47]). Since only one population of particles is observed, the following scenario is proposed: the larger voids nucleate early on the larger particles and grow significantly during the plastic deformation process and the smaller voids result from later nucleation on smaller particles with smaller opportunity to grow. The smallest voids probably nucleate during the void coalescence process leading to what resembles a void sheeting mechanism. By comparing Figs. 7(d) to Figs. 9(d), this scenario is amplified under shear conditions. Other reasons for differences in void growth rate could also play role as related to local microstructure, see *e.g.* [48].

2.4. Void nucleation characterization

The fractured 2PL specimens were polished down to mid-thickness. SEM micrographs of the microstructure were taken at different distances from the fracture surface following the approach employed in [47, 46]. The porosity distribution is then determined as a function of the distance from the crack surface as shown in Fig. 10. No voids are found in the undeformed material. Under loading, cavities are nucleated by the matrix-inclusion decohesion. These cavities have no preferential orientation and nucleate at the early stage of the plastic deformation. In the modeling part, we will therefore assume that the voids are initially present with an initial porosity equal to 0.002 (corresponding to the measured inclusion content). This average value is found far from the fracture surface as shown in Fig. 10 hence confirming the validity of the assumptions that each inclusion leads to one cavity.

2.5. Summary of the experimental behavior of CoCrNi

From the experimental study performed on the different specimen geometries with the CoCrNi high entropy alloy, the following observations can be made:

1. The CoCrNi high entropy alloy is very ductile with a high fracture strain over a wide range of stress states.

2. Under tensile loading conditions, the fracture behavior follows a ductile mechanism involving different stages of void evolution. The shear localization and internal necking fracture modes are observed.

3. The stress triaxiality and Lode variable both impact the fracture behavior. At constant Lode variable, ductility decreases with increasing triaxiality. The Lode variable strongly affects the fracture mode and the fracture surface morphology.
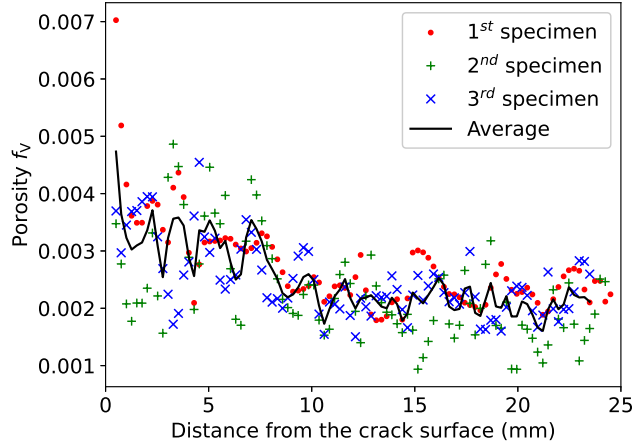
14

Figure 10: Porosity distribution in terms of the distance to the fracture surface: the measurements are performed post-mortem on three different 2PL specimens.

In the next sections, the nonlocal ductile fracture model developed in [41] is considered to address the different effects and mechanisms involving shear localization and internal necking dominated void coalescence phenomena.

3. Numerical modeling framework

The nonlocal ductile fracture model developed in [41] is employed to capture the complex behavior of the high entropy alloys. The constitutive model in the finite strain setting is expressed as the first Piola-Kirchhoff stress tensor (denoted by $\mathbf{P}$) being a function of the deformation gradient tensor (denoted by $\mathbf{F}$) and a set of internal variables $\mathbf{Z}$ to capture the history dependence as

$$\mathbf{P} = \mathfrak{P}\left(\mathbf{F}, \mathbf{Z}\right) , \text{ and evolution laws for } \mathbf{Z} . \tag{6}$$

In this work, we assume isotropic and isothermal behavior. In addition, all the experimental tests mentioned in Section 2.2 were performed at constant cross-head velocity of 1 mm/min, leading to an engineering strain rate varying from $10^{-4} s^{-1}$ to $10^{-3} s^{-1}$. Since these values are small enough to consider those tests being in quasi-static (see *e.g.* [49, 50]), a rate-independent modeling framework has been selected.

3.1. Voids morphology

The mechanical behavior of the porous medium depends on the geometry and distribution of voids, which are characterised by different effective parameters. In this work, we assume that

1. during the growth phase, voids are initially spherical and do not depart significantly from their initial shape, and,
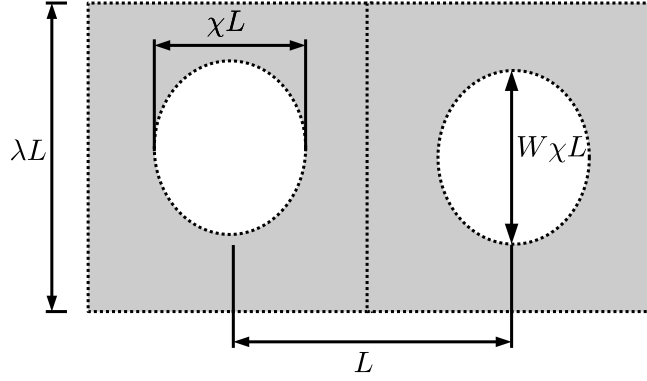
15

Figure 11: Geometrical parameters of periodic cylindrical unit cells where each cell includes a spheroidal void at its centre: the void aspect ratio W, void ligament ratio χ, and void spacing ratio λ.

2. during the coalescence phase, the void axes are attached to a coordinate system defined by the principle stress directions, and the voids maintain spheroidal shapes [41].

As a result, the geometry of such a unit cell is completely determined by several dimensionless variables: the porosity f, the void aspect ratio W, the void ligament ratio χ, the void spacing ratio λ, see Fig. 11 for the description of a representative cylindrical unit cell embedding a void at its centre. These void characteristics are related by the following relationship

$$f = \frac{2\chi^3 W}{3\lambda} \,. \tag{7}$$

To describe the void characteristics, a set of parameters $\mathbf{Y}$ is set as

$$\mathbf{Y} = \begin{bmatrix} f & \chi & W & \lambda \end{bmatrix}^T \,. \tag{8}$$

Voids are assumed to be present from the beginning with initial values $\mathbf{Y}_0 = \begin{bmatrix} f_0 & \chi_0 & W_0 & \lambda_0 \end{bmatrix}^T$ with $W_0 = 1$ and $\chi_0 = (1.5 f_0 \lambda_0)^{\frac{1}{3}}$, which correspond to initially spherical voids. In the next section, the evolution laws for 3 out of 4 variables in $\mathbf{Y}$ are provided for each phase of void evolution, and Eq. (7) is used to estimate the remaining parameter. Since each mechanism in the void evolution provides the evolution laws of these variables separately, it is convenient to keep the four porous plasticity parameters in the constitutive model.

3.2. Multi-yield surface multi-nonlocal variable micromechanics-based ductile failure model

The main elements of the ductile fracture model proposed in [41] are briefly recalled. The deformation gradient $\mathbf{F}$ is decomposed into the reversible elastic part $\mathbf{F}^e$ and the irreversible plastic part $\mathbf{F}^p$ such that

$$\mathbf{F} = \mathbf{F}^e \cdot \mathbf{F}^p \,. \tag{9}$$

16

The elastic potential energy is defined as

$$\rho_0 \psi^e(\mathbf{C}^e) = \frac{K}{2} \ln^2 J^e + \frac{G}{4} \mathrm{dev}\,(\ln \mathbf{C}^e) : \mathrm{dev}\,(\ln \mathbf{C}^e) \,, \tag{10}$$

where ρ_0 is the density, $\psi^e(\mathbf{C}^e)$ is the elastic potential energy per unit mass, $\mathbf{C}^e = \mathbf{F}^{eT} \cdot \mathbf{F}^e$, $J^e = \det \mathbf{F}^e$ is the elastic Jacobian, and K and G correspond to the bulk and shear moduli of the material, respectively. The first Piola-Kirchhoff stress tensor $\mathbf{P}$ derives from the elastic potential (10) for a given plastic state, yielding

$$\mathbf{P} = \rho_0 \frac{\partial \psi^e}{\partial \mathbf{F}}\bigg|_{\mathbf{F}^p} = K \mathbf{F}^{-T} \ln J^e + G \mathbf{F}^e \cdot \left[\mathbf{C}^{e-1} \cdot \mathrm{dev}\,(\ln \mathbf{C}^e)\right] \cdot \mathbf{F}^{p-T} \,. \tag{11}$$

Equation (10) leads to the following rate form

$$\rho_0 \dot{\psi}^e = \mathbf{P} : \dot{\mathbf{F}} = J \boldsymbol{\sigma} : \dot{\mathbf{E}}^e \,, \tag{12}$$

where $\mathbf{E}^e = \ln \sqrt{\mathbf{C}^e}$ is the elastic logarithmic strain tensor and $\boldsymbol{\sigma}$ is the corotational Cauchy stress. From Eq. (12), one has

$$\boldsymbol{\sigma} = \frac{1}{J} \mathbf{F}^{eT} \cdot \mathbf{P} \cdot \mathbf{F}^{pT} = \frac{1}{J} \mathbb{C} : \mathbf{E}^e \,, \tag{13}$$

where $\mathbb{C} = K\mathbf{I} \otimes \mathbf{I} + 2G \boldsymbol{\mathcal{I}}^{dev}$ in which $\boldsymbol{\mathcal{I}}^{dev}$ is the deviatoric part of the fourth order identity tensor.

The elastic part $\mathbf{F}^e$ and the plastic part $\mathbf{F}^p$ of the deformation gradient $\mathbf{F}$ are obtained following a porous plasticity model. In a general form, the porous plasticity model is summarised as follows:

$$\Phi = \Phi\left(\boldsymbol{\sigma}; \sigma_Y, \mathbf{Y}\right) \,, \tag{14}$$

$$\sigma_Y = \sigma_Y^0 + R\left(\varepsilon_m\right) \,, \tag{15}$$

$$\mathbf{D}^p = \dot{\mathbf{F}}^p \cdot \mathbf{F}^{p-1} = \dot{\mu} \frac{\partial \Phi}{\partial \boldsymbol{\sigma}} \,, \tag{16}$$

$$\boldsymbol{\sigma} : \mathbf{D}^p = (1-f)\,\sigma_Y \dot{\varepsilon}_m \,, \tag{17}$$

$$\dot{\mu} \geq 0 \,, \Phi \leq 0 \,, \dot{\mu}\Phi = 0 \,, \tag{18}$$

$$\dot{\bar{\varepsilon}}_m - \dot{\varepsilon}_m - l_m^2 \Delta_0 \dot{\bar{\varepsilon}}_m = 0 \,, \tag{19}$$

$$\dot{\bar{\varepsilon}}_v - \dot{\varepsilon}_v - l_v^2 \Delta_0 \dot{\bar{\varepsilon}}_v = 0 \text{ with } \dot{\varepsilon}_v = \mathrm{tr}\left(\mathbf{D}^p\right) \,, \tag{20}$$

$$\dot{\bar{\varepsilon}}_d - \dot{\varepsilon}_d - l_d^2 \Delta_0 \dot{\bar{\varepsilon}}_d = 0 \text{ with } \dot{\varepsilon}_d = \sqrt{\frac{2}{3} \mathrm{dev}\,(\mathbf{D}^p) : \mathrm{dev}\,(\mathbf{D}^p)} \,, \text{ and} \tag{21}$$

$$\dot{\mathbf{Y}} = \boldsymbol{\Psi}\left(\mathbf{Y}, \boldsymbol{\sigma}, \dot{\bar{\varepsilon}}_m, \dot{\bar{\varepsilon}}_v, \dot{\bar{\varepsilon}}_d\right) \,, \tag{22}$$

where Φ is the multi-yield surface function defined next; σ_Y is the mean yield stress of the matrix; σ_Y^0 is the initial yield stress; $R\left(\varepsilon_m\right)$ is the strain-hardening contribution; ε_m is the mean equivalent plastic strain of the matrix; $\mathbf{D}^p$ is the plastic strain rate; μ is the plastic multiplier; ε_v is the volumetric equivalent plastic strain; ε_d is the deviatoric equivalent plastic strain; $\bar{\varepsilon}_m$, $\bar{\varepsilon}_v$, and $\bar{\varepsilon}_d$ are respectively the nonlocal counterparts

of ε_{m}, ε_{v}, and ε_{d}; Δ_0 is the Laplace operator with respect to the reference configuration; $l = l_{\mathrm{m}} = l_{\mathrm{v}} = l_{\mathrm{d}}$ is the nonlocal length scale, which are assumed to be the same for the three nonlocal variables $\bar{\varepsilon}_{\mathrm{m}}$, $\bar{\varepsilon}_{\mathrm{v}}$, and $\bar{\varepsilon}_{\mathrm{d}}$; and $\boldsymbol{\Psi}$ denotes a set of evolution laws for void characteristics $\mathbf{Y}$. In this set of Eqs. (14 – 22):

- Eqs. (14 – 18) represents a system of equations typical of an elastoplastic model under finite strains. Eq. (14) represents a yield function, which is expressed in terms of the corotational Cauchy stress tensor $\boldsymbol{\sigma}$. Moreover, the effects of the porosity and of the void shape in the yield condition should be accounted for as described further in this paper. Eq. (15) represents the isotropic hardening. Eq. (16) represents the associative plastic flow rule. Eq. (17) represents the balance of the plastic dissipation in which the rate of apparent plastic work is equal to the rate of plastic work in the matrix [20, 21, 22]. The right hand side term $(1 - f)\,\sigma_{\mathrm{Y}}\dot{\varepsilon}_{\mathrm{m}}$ corresponds to an averaged measure of the plastic dissipation rate over the matrix material within the representative volume while the left hand side term $\boldsymbol{\sigma} : \mathbf{D}^{\mathrm{p}}$ corresponds to the macroscopic plastic dissipation. Under a localized state such as during void coalescence, the use of Eq. (17) seems to underestimate the flow stress in the localization region. Despite its approximate nature, Eq. (17) was used in most studies [17] because it incorporates the isotropic hardening effect as an additional equation governing the evolution of ε_{m}. And Eq. (18) governs the loading-unloading conditions.

- Eqs. (19, 20, 21) correspond to the additional Helmholtz-type boundary value problem allowing the nonlocal variables to be estimated from their local counterparts [51]. They are monolithically solved with the classical mechanical equations in a fully coupled form [41].

- Eq. (22) describes the evolution laws for the void characteristics $\mathbf{Y}$, which are driven by the nonlocal variables.

The porous plastic model employed in this work consists in the competition between the three modes of porosity evolution. First, the diffuse void growth phase is governed by the Gurson–Tvergaard–Needleman (GTN) yield function (denoted by Φ_{G}) and the corresponding evolution laws for the void characteristics (denoted by $\boldsymbol{\Psi}_{\mathrm{G}}$). Secondly, the internal necking void coalescence is governed by the extended Thomason yield function (denoted by Φ_{T}) and the corresponding evolution laws for the void characteristics (denoted by $\boldsymbol{\Psi}_{\mathrm{T}}$). Thirdly, the shear-driven void coalescence is governed by the shear-driven yield function (denoted by Φ_{S}) and the corresponding evolution laws for the void characteristics (denoted by $\boldsymbol{\Psi}_{\mathrm{S}}$). Mathematically,

one considers the yield surface (14) and evolution laws for void characteristics (22) as follows

$$\Phi = \max\left(\Phi_\mathrm{G}, \Phi_\mathrm{T}, \Phi_\mathrm{S}\right) \text{ and} \tag{23}$$

$$\begin{cases} \boldsymbol{\Psi} = \boldsymbol{\Psi}_\mathrm{G} & \text{during void growth}, \\ \boldsymbol{\Psi} = \boldsymbol{\Psi}_\mathrm{T} & \text{during internal necking coalescence}, \text{ and} \\ \boldsymbol{\Psi} = \boldsymbol{\Psi}_\mathrm{S} & \text{during shear-driven coalescence}. \end{cases} \tag{24}$$

Additionally, the onset of the internal necking coalescence is detected by

$$\dot{\varepsilon}_\mathrm{m} > 0 \text{ and } \Phi_\mathrm{T} > \max\left(\Phi_\mathrm{G}, \Phi_\mathrm{S}\right), \tag{25}$$

while the onset of the shear-driven coalescence is detected by

$$\dot{\varepsilon}_\mathrm{m} > 0 \text{ and } \Phi_\mathrm{S} > \max\left(\Phi_\mathrm{G}, \Phi_\mathrm{T}\right). \tag{26}$$

We assume that void coalescence cannot switch from one mode to another. As a result, the evolution laws for the void characteristics during coalescence follow the ones of the coalescence mode whose onset condition is first met in the loading history.

A fully implicit integration scheme of the porous plasticity model described by Eqs. (14–22) can be performed as detailed in [41]. In the following, the yield surfaces and the corresponding evolution laws for the different modes are summarised.

3.2.1. Void growth phase

The GTN yield function is expressed as

$$\Phi_\mathrm{G} = \frac{\hat{\sigma}_\mathrm{G}}{\sigma_\mathrm{Y}} - 1 \text{ with } \hat{\sigma}_\mathrm{G}\left(\sigma_\mathrm{eq}, p', \sigma_\mathrm{Y}, f\right) = \frac{\sqrt{\sigma_\mathrm{eq}^2 + 2\sigma_\mathrm{Y}^2 f q_1 \left[\cosh\left(\frac{3}{2} q_2 \frac{p'}{\sigma_\mathrm{Y}}\right) - 1\right]}}{1 - q_1 f}, \tag{27}$$

$$\sigma_\mathrm{eq} = \sqrt{\frac{3}{2}\mathrm{dev}\left(\boldsymbol{\sigma}\right) : \mathrm{dev}\left(\boldsymbol{\sigma}\right)}, \text{ and } p' = \frac{\mathrm{tr}\left(\boldsymbol{\sigma}\right)}{3}, \tag{28}$$

where $\hat{\sigma}_\mathrm{G}$ denotes the GTN effective stress, σ_eq is the von Mises equivalent stress, p' is the hydro-static stress, and q_1 and q_2 are two material parameters.

Under the assumption that there is no void nucleation, the voids initially exist and they remain spherical

19

during the void growth phase. The evolution laws for the void characteristics $\mathbf{Y}$ then read

$$
\boldsymbol{\Psi}_{\mathrm{G}} : \begin{cases}
\dot{f} = (1 - f)\dot{\bar{\varepsilon}}_{\mathrm{v}} + k_\omega \phi_\eta \phi_\omega f \dot{\bar{\varepsilon}}_{\mathrm{d}} , \\[1mm]
\dot{W} = 0 , \\[1mm]
\dot{\lambda} = \kappa \lambda \dot{\bar{\varepsilon}}_{\mathrm{d}} , \text{ and} \\[1mm]
\dot{\chi} = \dfrac{\chi}{3} \left(\dfrac{\dot{f}}{f} - \dfrac{\dot{W}}{W} + \dfrac{\dot{\lambda}}{\lambda} \right) ,
\end{cases}
\tag{29}
$$

with $\phi_\eta = \exp\left[-\dfrac{1}{2}\left(\dfrac{\eta}{\eta_s}\right)^2 \right]$, $\phi_\omega = 1 - \omega^2$, $\eta = \dfrac{p'}{\sigma_{\mathrm{eq}}}$ and $\omega = \dfrac{27 \det\left(\mathrm{dev}\left(\boldsymbol{\sigma}\right)\right)}{2\sigma_{\mathrm{eq}}{}^3}$, $\tag{30}$

where k_ω is the shear-accelerated void growth factor [30], η_s is a user parameter, and κ is the void spacing control factor which depends on the distribution of voids [17]. In more details, in Eq. (29),

- In the absence of voids nucleation, the evolution of f consists of the void growth contribution $\dot{f}_{\mathrm{gr}} = (1 - f)\dot{\bar{\varepsilon}}_{\mathrm{v}}$ associated to the plastic incompressibility of the matrix [21, 22] and the shear contribution $\dot{f}_{\mathrm{sh}} = k_\omega \phi_\eta \phi_\omega f \dot{\bar{\varepsilon}}_{\mathrm{d}}$ corresponding to an effective change of porosity due to void deformation (through ϕ_η) and reorientation occurring under shear-dominated distortions (through ϕ_ω) [30]. Since the choice in [30] of ϕ_η equal to 1 and $\phi_\omega = 1 - \omega^2$ can degrade the prediction accuracy of the void growth under high stress triaxiality, in the present work, ϕ_η and ϕ_ω respectively take the forms expressed in Eq. (30) where ϕ_η is close to 1 at very low stress triaxiality and vanishes at high stress triaxiality.

- The void spacing ratio λ evolves from its initial value λ_0 and is controlled by the plastic deformation as proposed in [36, 52, 17].

- The evolution law of χ is obtained from the rate form of Eq. (7).

3.2.2. Internal necking coalescence mode

The extended Thomason yield function proposed in [41] to account for the Lode angle is expressed as

$$
\Phi_{\mathrm{T}} = \frac{\hat{\sigma}_{\mathrm{T}}}{\sigma_{\mathrm{Y}}} - 1 \text{ with } \hat{\sigma}_{\mathrm{T}} = \frac{1}{C_{\mathrm{Tf}}}\left(s_1 + |p'|\right), s_1 = \frac{2}{3}\sigma_{\mathrm{eq}}\cos\theta, \text{ and } \theta = \frac{1}{3}\arccos\omega ,
\tag{31}
$$

where $\hat{\sigma}_{\mathrm{T}}$ denotes the Thomason effective stress, s_1 is the maximum principal deviatoric stress, $\theta \in \left[0 \ \dfrac{\pi}{3}\right]$ is the Lode angle, and C_{Tf} is the the load concentration factor

$$
C_{\mathrm{Tf}}\left(W, \chi\right) = \left(1 - \chi^2\right)\left[h\left(\frac{1 - \chi}{W\chi}\right)^2 + g\sqrt{\frac{1}{\chi}} \right] ,
\tag{32}
$$

with h and g being two constants. The value of h should be calibrated as a function of the representative strain hardening exponent of the matrix and $g = 1.24$ [32].

The evolution laws for void characteristics $\mathbf{Y}$ under the internal necking coalescence mode are deduced from the plastic incompressibility of the matrix following the work of [36] as

$$\boldsymbol{\Psi}_{\mathrm{T}} : \begin{cases} \dot{\chi} = \dfrac{3}{4}\dfrac{\lambda}{W}\left(\dfrac{3}{2\chi^2} - 1\right)\dot{\bar{\varepsilon}}_{\mathrm{d}}\,, \\[3mm] \dot{W} = \dfrac{9}{4}\dfrac{\lambda}{\chi}\left(1 - \dfrac{1}{2\chi^2}\right)\dot{\bar{\varepsilon}}_{\mathrm{d}}\,, \\[3mm] \dot{\lambda} = \kappa\lambda\dot{\bar{\varepsilon}}_{\mathrm{d}}\,,\ \text{and} \\[3mm] \dot{f} = f\left(3\dfrac{\dot{\chi}}{\chi} + \dfrac{\dot{W}}{W} - \dfrac{\dot{\lambda}}{\lambda}\right)\,, \end{cases} \tag{33}$$

in which the evolution of λ is the same as the one during the void growth phase, and the last equation is obtained from the rate form of Eq. (7).

3.2.3. Shear-driven coalescence mode

The shear-driven yield function is expressed in terms of the maximum shear stress [41] as

$$\Phi = \Phi_{\mathrm{S}} = \frac{\hat{\sigma}_{\mathrm{S}}}{\sigma_{\mathrm{Y}}} - 1 \ \text{with}\ \hat{\sigma}_{\mathrm{S}} = \frac{\sqrt{3}}{2}\frac{s_1 - s_3}{C_{\mathrm{Sf}}}\,, s_1 = \frac{2}{3}\sigma_{\mathrm{eq}}\cos\theta\,, \ \text{and}\ s_3 = \frac{2}{3}\sigma_{\mathrm{eq}}\cos\left(\theta + \frac{2\pi}{3}\right)\,, \tag{34}$$

where $\hat{\sigma}_{\mathrm{S}}$ denotes the effective shear stress, s_1 and s_3 are respectively the maximum and minimum principal deviatoric stresses, and C_{Sf} denotes the shear load factor

$$C_{\mathrm{Sf}} = \xi\left(1 - \chi^2\right)\,, \tag{35}$$

with $\xi \geq 1$ being introduced to capture the onset of shear-driven coalescence.

Since only χ affects the material response during a shear-driven coalescence deformation mode, the evolution laws of f, W, and λ do not have to be considered. Consequently, the evolution laws for void characteristics $\mathbf{Y}$ under the shear-driven coalescence are given as

$$\boldsymbol{\Psi}_{\mathrm{S}} : \begin{cases} \dot{f} = 0 \\[2mm] \dot{\chi} = K_{\chi}\dot{\bar{\varepsilon}}_{\mathrm{d}}\,, \\[2mm] \dot{W} = 0\,,\ \text{and} \\[2mm] \dot{\lambda} = \dfrac{3\lambda\dot{\chi}}{\chi}\,, \end{cases} \tag{36}$$

in which K_{χ} is the acceleration factor of the void ligament under the shear-driven coalescence mode, and the last equation is obtained from the rate form of Eq. (7). Under the shear-driven coalescence deformation mode, the void ligaments are flattened and elongated following the shearing direction until neighbouring voids coalesce by plastic flow localization [53]. This motivates the use of an evolution law driven by the

deviatoric equivalent plastic strain $\bar{\varepsilon}_d$. In this modeling framework, the evolution of χ follows a simple phenomenological law driven by the plastic deformation under a constant growth rate K_χ for simplicity. In future works, more physics-based evolution laws will be elaborated.

3.3. Summary

Since it was observed in Section 2 that the voids nucleate at the very beginning of the loading by matrix inclusions decohesion, it is assumed that the voids are initially spherical and present from the beginning with an initial porosity f_0 ($= 0.002$) and the initial geometrical parameters given as $W_0 = 1$, $\lambda_0 = 1$ and $\chi_0 = (1.5 f_0 \lambda_0)^{\frac{1}{3}}$. To model ductile fracture, three modes of plasticity driven porosity evolution are considered, namely

1. diffuse void growth (GTN),
2. internal necking void coalescence (extended Thomason), and
3. shear-driven void coalescence.

In addition, three distinct coupled models can be employed:

1. the coupled GTN-Thomason model by setting $\xi \to +\infty$ to prohibit shear-driven coalescence,
2. the coupled GTN-Shear model by setting $g \to +\infty$ to prohibit internal necking coalescence, and
3. the fully coupled GTN-Thomason-Shear model (denoted by GTN-Th-Sh model in the following sections).

The list of parameters to be identified is summarised in Tab. 2. In the next section, the parameters of the coupled GTN-Thomason-Shear model are calibrated for the CoCrNi high entropy alloy from the results of the experimental campaign conducted in Section 2.

4. Parameter identification and model validation

In this section, the finite element models of the different test specimens are first described. Then the material parameters, reported in Tab. 2, of the multi-yield surface multi-nonlocal variable micromechanics-based ductile failure model are identified. To this end, since the different geometries correspond to different stress states and trigger different failure modes, the parameters related to different modes are identified using the most appropriate geometries. When different shape factors have been tested for a given family of sample geometry, like for the 2NSx and 7GRx families, only one shape factor is considered during the identification process so that the other ones can be used for validation.

Table 2: Material parameters of the multi-yield surface multi-nonlocal variable micromechanics-based ductile failure model to be calibrated.

Parameter	Unit (SI)	Meaning
ρ_0	$\mathrm{kg \cdot m^{-3}}$	Density
K	Pa	Bulk modulus (see Eq. (10))
G	Pa	Shear modulus (see Eq. (10))
σ_Y^0	Pa	Initial yield stress (see Eq. (15))
R	Pa	Strain hardening stress (see Eq. (15))
f_0	-	Initial porosity
q_1, q_2	-	GTN coefficients (see Eq. (27))
k_ω	-	Shear-controlled void growth factor (see Eq. (29))
η_s	-	η-limited shear-controlled void growth (see Eqs. (29, 30))
κ	-	Void spacing control factor (see Eq. (29, 33))
h, g	-	C_Tf coefficients (see Eq. (32))
ξ	-	C_Sf coefficient (see Eq. (35))
K_χ	-	Ligament shrinkage rate under shear (see Eq. (36))
l_m, l_v, l_d	m	Nonlocal lengths (see Eqs. (19 – 21))

4.1. Finite element models of the specimens

The plate specimens (1L, 2PL, 2NS4, 2NS2, 2NS1, and 3SHEAR) are discretised with 3-dimensional 10-node tetra elements, see Fig. 12(a)-(f). The symmetries of the geometry and of loading conditions are exploited. One half of the specimens are considered for the 1L, 2PL, 2NS4, 2NS2, and 2NS1 geometries; however the symmetry of these specimens through the thickness direction cannot be exploited in order to capture the slant fracture mode. The symmetry of the specimen following the thickness direction is exploited for the 3SHEAR geometry, leading to modeling a quarter of the specimen for this case. The axisymmetric specimens (4SR and 5NR1) are modeled with axisymmetric finite elements using 6-node triangles, see Fig. 12(g) and (h). The plane strain grooved specimens (7GR1, 7GR3, and 7GR6) are modeled in a two-dimensional plane strain formulation and are meshed using 6-node triangle elements, see Fig. 12(i)-(k). Fig. 12 shows the finite element meshes. All meshes are refined in the necking or notched regions in order to better capture high local strain gradient. In addition, the sensitivity of the mesh size is systematically performed to ensure the convergence of numerical results upon mesh refinement.

4.2. Parameters identification

The parameters of the constitutive model reported in Tab. 2 are calibrated in this section for the CoCrNi alloy using an inverse procedure to fit the experimental and numerical force-displacement responses. These parameters are divided into the following different groups:

1. The elastoplastic parameters consist of the elastic compressibility and shear moduli, K and G respectively, and the description of the hardening law provided under a functional form $\sigma_{\mathrm{Y}} = \sigma_{\mathrm{Y}}^0 + R\left(\varepsilon_{\mathrm{m}}\right)$;

2. The porous-related parameters: f_0, q_1, q_2, k_ω, η_s, κ, h, g, ξ, and K_χ; and

3. The nonlocal characteristic lengths: l_{m}, l_{v}, and l_{d}.

The elastoplastic parameters are calibrated using the smooth plate specimen (1L) in combination with one notched round specimen (5NR4). The parameters f_0 and the nonlocal characteristic lengths are identified from microstructure characterization based on the measurement of the porosity distribution after fracture of the tapered sample (2PL). The remaining parameters are identified using 5NR4, the shear specimen (3SHEAR), and one grooved plate (7GR3), in combination with several assumptions often advocated in ductile fracture modeling.

4.2.1. The elastoplastic parameters

At low initial porosity, the effect of the porosity on the global stress-strain curve prior to the fracture is negligible. As a result, the tensile tests performed on smooth specimens are often used to identify the elastoplastic parameters since the hardening curve can be directly extracted from the experimental stress

(a) 1L   (b) 2PL   (c) 2NS4   (d) 2NS2   (e) 2NS1   (f) 3SHEAR

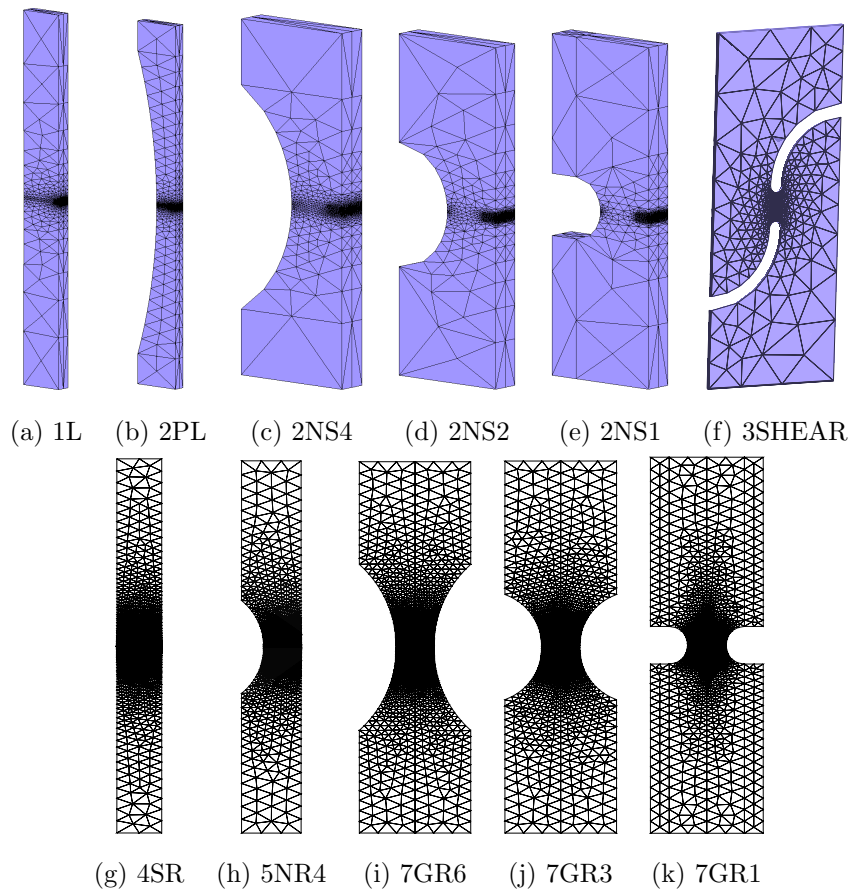(g) 4SR   (h) 5NR4   (i) 7GR6   (j) 7GR3   (k) 7GR1

Figure 12: Finite element meshes for simulations: (a) 1L, (b) 2PL, (c) 2NS4, (d) 2NS2, (e) 2NS1, (f) 3SHEAR, (g) 4SR, (h) 5NR4, (i) 7GR1, (j) 7GR3, and (k) 7GR6.
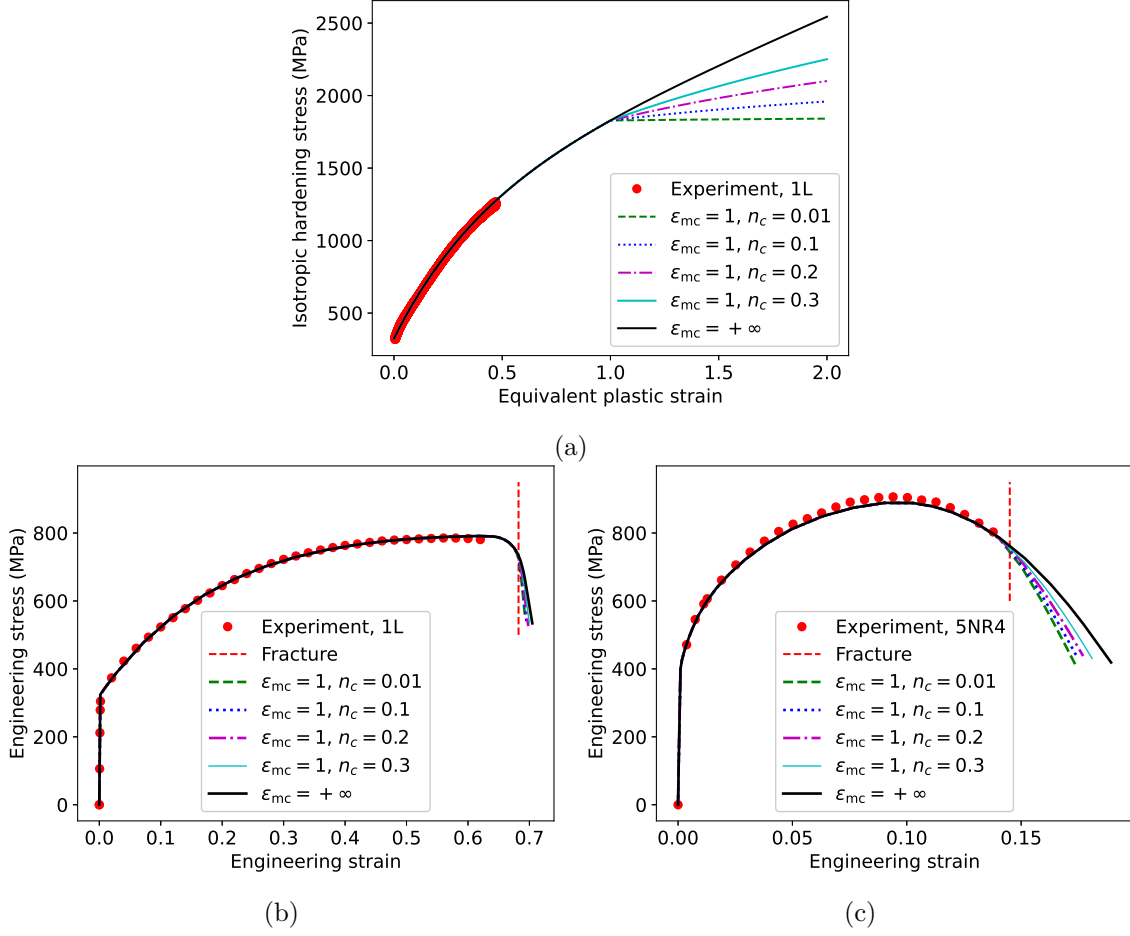
Figure 13: Comparison of the numerical stress-strain responses predicted by the elastoplastic model with the experimental results: (a) hardening curves, and (b, c) the corresponding responses obtained for respectively the 1L and the 5NR4 samples. Experimental results of the 1L and the 5NR4 samples reported in Fig. 4 are shown with corresponding average responses for comparison purposes.

strain curves[4]. The corresponding hardening curves are extracted from the experimental engineering stress-strain data obtained with 1L prior to the onset of necking and reported in Fig. 13(a). However, the maximum value of the plastic strain is ≈ 0.5. The hardening curve in a higher plastic strain level is identified using the experimental data obtained with the 5NR4 specimens through an inverse procedure.

---

[4]The experimental data of the tensile tests on the smooth specimens are generally provided as the applied force F versus a gauge length L during loading. This result is converted to the true stress-strain curve according to the following formula $\sigma = \frac{F}{A_0}\left(1 + \frac{L-L_0}{L_0}\right)$ and $\varepsilon = \ln \frac{L}{L_0}$, where A_0 is the initial cross section of the specimen and L_0 is the initial gauge length. The plastic strain is then estimated using the relation $\sigma = E\left(\varepsilon - \varepsilon_{\mathrm{m}}\right)$ where E is the Young modulus. As a result, the hardening curve $\sigma = \sigma\left(\varepsilon_{\mathrm{m}}\right)$ can be deduced.

The hardening curve described by Eq. (15) is assumed to take the following form

$$
\sigma_{\mathrm{Y}}\left(\varepsilon_{\mathrm{m}}\right)=
\begin{cases}
\sigma_{\mathrm{Y}}^{0}+h_{1}\varepsilon_{\mathrm{m}}+h_{2}\left[1-\exp\left(-\dfrac{\varepsilon_{\mathrm{m}}}{h_{\exp}}\right)\right] & \text{if } \varepsilon_{\mathrm{m}} \leq \varepsilon_{\mathrm{m}c} \\[2ex]
\sigma_{\mathrm{Y}c}\left(\dfrac{\varepsilon_{\mathrm{m}}}{\varepsilon_{\mathrm{m}c}}\right)^{n_{c}} & \text{if } \varepsilon_{\mathrm{m}} > \varepsilon_{\mathrm{m}c},
\end{cases}
\tag{37}
$$

where σ_{Y}^{0}, h_{1}, h_{2}, $h_{\exp}$, $\varepsilon_{\mathrm{m}c}$ and n_{c} need to be identified. The parameters $\varepsilon_{\mathrm{m}c}$ and n_{c} are introduced in order to capture the saturation of strain hardening at very large high plastic strain. The value σ_{Y}^{0} can be directly obtained from the experimental data of the 1L samples. The remaining parameters are obtained by fitting the engineering stress-strain response of the 5NR4 samples under the constraint that, at low plastic strain (< 0.5), the hardening curve matched the experimental true stress-true strain curves of the 1L sample. Only the experimental response up to the point of necking of the 1L specimen and the one before the fracture of the 5NR4 specimen are considered. Consequently, the values $\sigma_{\mathrm{Y}}^{0} = 325$ MPa, $h_{1} = 645$ MPa, $h_{2} = 935$ MPa, and $h_{\exp}=0.4$ are obtained.

However, none of the experimental results obtained with the 1L and 5NR4 specimens can be used to identify the hardening behavior when $\varepsilon_{\mathrm{m}} > \varepsilon_{\mathrm{m}c} = 1$ since fracture occurs before. Fig. 13 shows the comparison between the finite element predictions with the experimental tests. The effect of n_{c} on the engineering stress-strain curves is also shown. When $\varepsilon_{\mathrm{m}} \leq 1$, a good agreement is observed. In the large plastic strain range, i.e. $\varepsilon_{\mathrm{m}} > 1$, the void evolution needs to be incorporated into the constitutive model. In this work, we assume that the isotropic hardening stress is almost saturated when $\varepsilon_{\mathrm{m}} > 1$ by considering $n_{c} = 0.01$. The porous-plasticity parameters are then identified accordingly.

4.2.2. Porous-plasticity parameters

In this work, we employ the conventional values of $q_{1} = 1.5$ and $q_{2} = 1$ [54]. For the parameters g and h of the Thomason model, the values $g = 0.1$, and $h = 1.24$ are selected [32]. In addition, we assume that k_{ω} only has a considerable effect at low stress triaxiality by setting $\eta_{s} = 0.15$, i.e. the contribution of k_{ω} in Eq. (29) vanishes when the stress triaxiality is larger than 0.5. This corresponds to the Nahshon-Hutchinson shear term improvement proposed by [55]. Under this assumption, k_{ω} has almost no effect on the numerical response for the grooved plates (7GRx). As a result, the remaining parameters f_{0}, k_{ω}, κ, ξ, and K_{χ} are identified as follows:

1. The initial porosity f_{0} is chosen by microstructure characterization from the measurement of the porosity distribution in the progressive notched plate (2PL) after fracture, as reported in Section 2.4.

2. The void spacing factor κ is identified in order to exactly capture the fracture point of the notched round bar (5NR4) since, for the 5NR4 specimens, fracture initiates by an internal necking coalescence

mode, in which case the remaining unknown parameters, including k_ω, ξ, and k_χ, have almost no effect on the numerical response.

3. The shear coalescence parameters ξ and k_χ are identified in order to exactly capture the fracture point observed on the grooved plate (7GR3) in which the effect of k_ω is almost negligible due to high stress triaxiality state.

4. The shear-controlled void growth parameter k_ω is identified based on the shear sample (3SHEAR) using all other parameters which have already been identified.

Porosity evolution parameter (f_0): The distribution of the porosity was measured on the tapered specimen (2PL) with respect to the distance to the crack surface, see Fig. 10. As a result, we consider the following assumption: the voids are initially spherical with the initial porosity $f_0 = 2 \times 10^{-3}$ and the other void characteristics are set as $W_0 = 1$, $\lambda_0 = 1$, and $\chi_0 = \left(\dfrac{3 f_0 \lambda_0}{2} \right)^{\frac{1}{3}} = 0.1442$.

Nonlocal lengths ($l_\mathbf{m}$, $l_\mathbf{v}$, $l_\mathbf{d}$): For simplicity, we assume that the nonlocal lengths are identical for all nonlocal variables, *i.e.*

$$l_\mathrm{m} = l_\mathrm{v} = l_\mathrm{d} = l \,. \tag{38}$$

The nonlocal length l is chosen as equal to 40 μm. This parameter affects the damage and fracture behavior, so the porous-plasticity parameters are identified accordingly. The value of l should be representation of the inter-distance of the relevant length scale associated to the damage process [56]. A value of 40 μm is approximately twice the average inter-void spacing. The nonlocal length value affects the localization process, not only, in the width of the location band, but also, in the localization patterns, *e.g.* for a given specimen size, larger characteristic lengths favor thicker localization band and flat crack advance [57]. However, as shown later in Section 4.3, this physically motivated choice of the nonlocal lengths leads to numerical predictions in reasonable agreement with the experimental measurements.

Internal necking parameters (κ): In the notched round bar (5NR4) test, fracture starts at the centre of the specimen by the coalescence of many voids following a flat internal necking type mechanism. The value of the void spacing factor $\kappa = 1.25$ produces a good match with the engineering strain at fracture of the 5NR4 test as shown in Fig. 14.

Shear coalescence parameters (ξ and K_χ): The grooved plate 7GR3 test is used to identify the C_Sf coefficient ξ and the ligament growth rate under shear parameter K_χ. Fig. 15 shows the influence of ξ and K_χ on the mechanical response. The value of ξ governs the onset of the coalescence while the value of K_χ governs the softening during the post coalescence response. As shown in Figs. 15, the values $\xi = 1.15$ and $K_\chi = 5$ are chosen, providing a fracture point in good agreement with the experimental fracture strain.
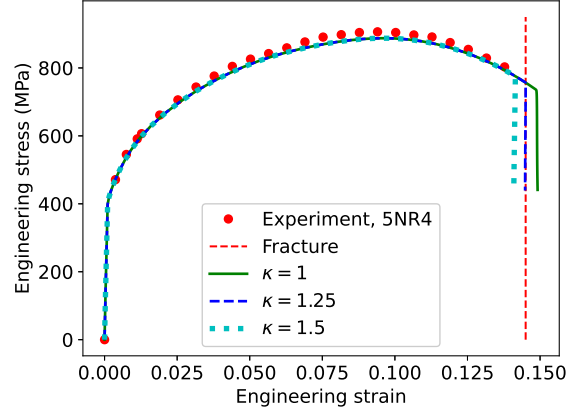
Figure 14: Influence of the void spacing control factor κ on the response of the 5NR4 specimen. The numerical simulations consider the coupled GTN-Thomason model. The engineering strain at fracture of the 5NR4 test is also reported. Only the average responses of the experimental results of Fig. 4 are reported for readability purpose.
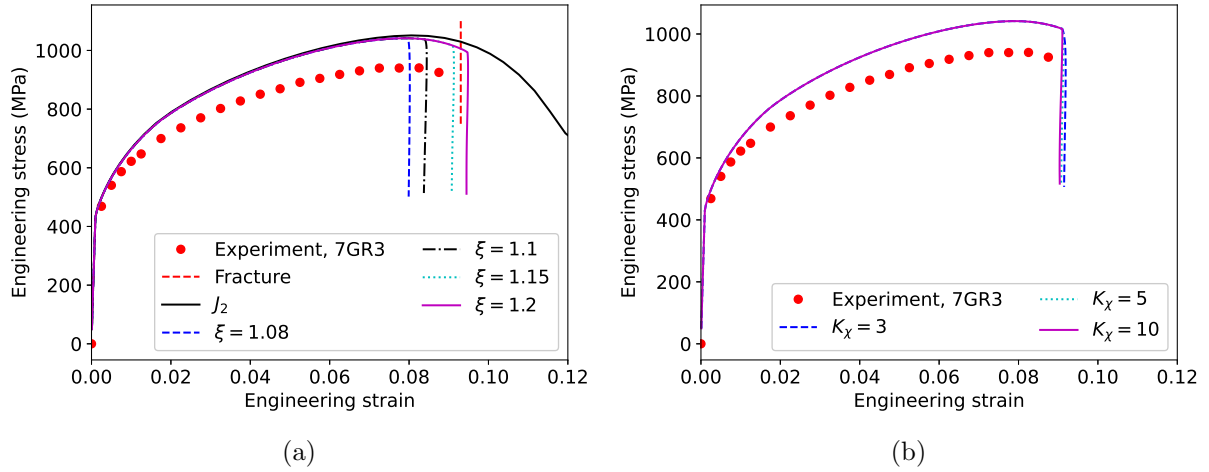

(a)   (b)

Figure 15: Influence of ξ and K_χ on the 7GR3 test: (a) influence of ξ with $K_\chi = 5$, and (b) influence of K_χ with $\xi = 1.15$. Only the average responses of the experimental results of Fig. 4 are reported for readability purpose. The elastoplastic and experimental responses are also reported for comparison.

29
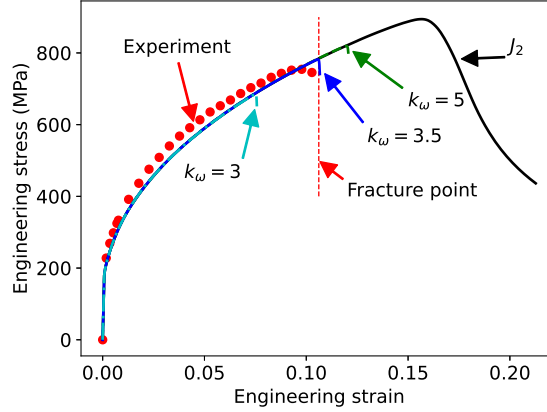
Figure 16: Influence of the shear-controlled void growth factor k_ω on the engineering stress-strain response of the 3SHEAR sample. The elastoplastic and experimental responses are also reported for comparison. Only the average responses of the experimental results of Fig. 4 are reported for readability purpose.

The shear-controlled void growth parameter (k_ω): The last parameter, the shear-controlled void growth factor k_ω, is identified using the shear sample (3SHEAR) such as to capture the fracture point on the experimental stress-strain curve. Fig. 16 shows the engineering stress-strain curve for different values of k_ω. The experimental results and the J_2 plasticity prediction (without damage) are also reported for comparison. The parameter k_ω has almost no effect on the behavior prior to fracture due to the low level of porosity. The value $k_\omega = 3.5$ is selected.

4.2.3. Hardening behavior when $\varepsilon_m > 1$

The identification procedure was performed by considering that the isotropic hardening stress is almost saturated with $n_c = 0.01$ when $\varepsilon_m > 1$. As shown in Fig. 17, in which the GTN-Th-Sh model with the identified parameters is considered, the post hardening behavior at large strain $\varepsilon_m > 1$ does not affect the overall mechanical response. The absence of plastic hardening could favor plastic localization. Indeed, as shown in Fig. 17(d) for the case of the 1L sample, the use of $n_c = 0.01$ favors inclined plastic localization bands, which is consistent with the slant fracture mode observed in this test, while a the case with $\epsilon_{mc} = +\infty$ favors flat localization band. We thus choose the values $\epsilon_{mc} = 1$ and $n_c = 0.01$ for the subsequent analyses.

4.2.4. Summary

The identified parameters are reported in Tab. 3. In the next section, the multi-yield surface multi-nonlocal variable micromechanics-based ductile failure model or GTN-Th-Sh model with the identified parameters is used to simulate all the experimental tests.

30

(a)

(b)

(c)

(d)
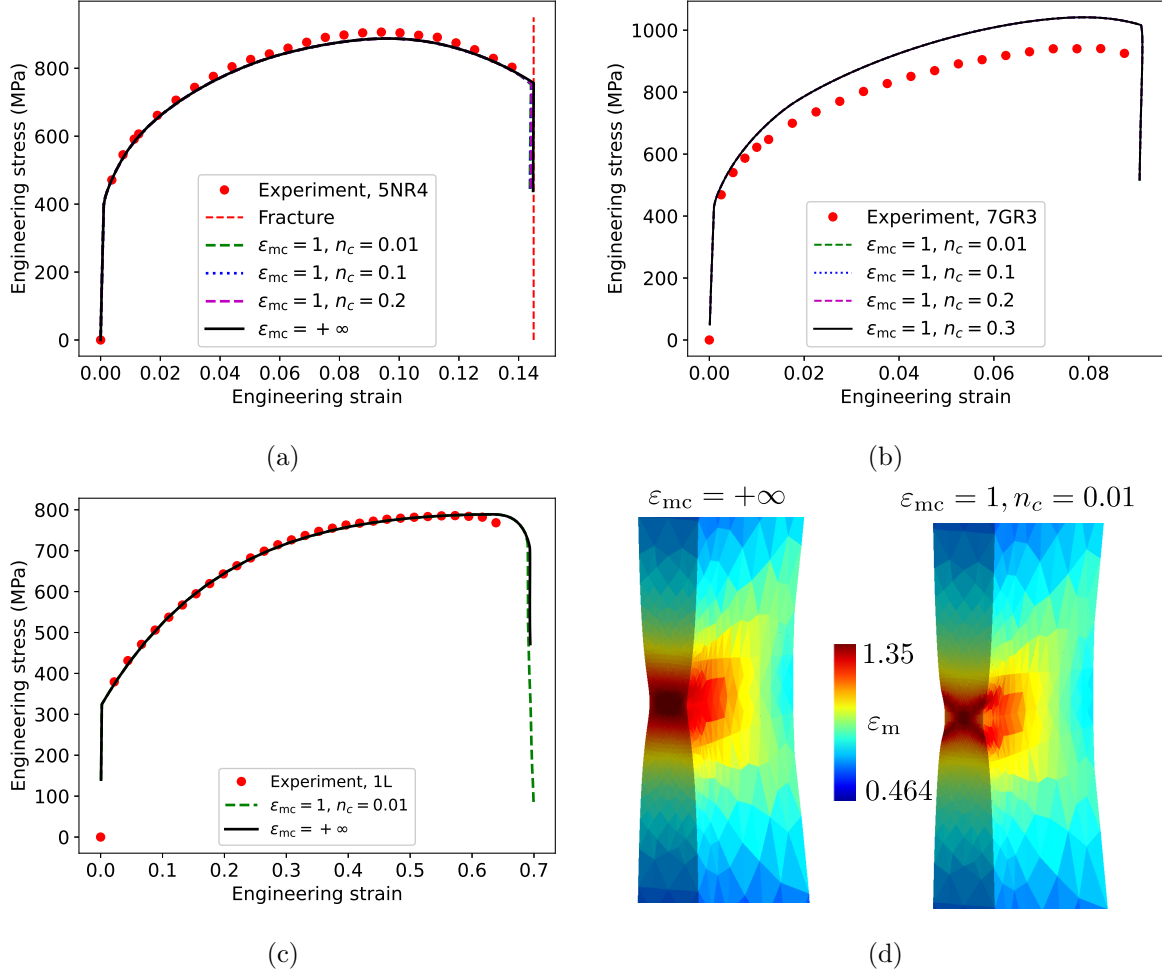
Figure 17: Influence of $\varepsilon_{\mathrm{m}c}$ on the engineering responses of (a) 5NR4, (b) 7GR3, (c) 1L tests, and (d) on the distribution of the plastic localization after onset of coalescence in the 1L test. The GTN-Th-Sh model with the identified parameters is considered. The average responses of the experimental results of Fig. 4 are also reported for readability purpose.

Table 3: Identified parameters of the multi-yield surface multi-nonlocal variable micromechanics-based ductile failure model.

Density	ρ_0 (kg · m^{-3})								
	8260								
Elastoplastic parameters	K (GPa)	G (GPa)	σ_{Y}^0 (MPa)	h_1 (MPa)	h_2 (MPa)	$h_{\exp}$	$\varepsilon_{\mathrm{m}c}$	n_c	
	176.83	81.62	325	645	935	0.4	1	0.01	
Porous-related parameters	f_0	q_1	q_2	k_ω	η_s	κ	h	g	ξ	K_χ
	0.002	1.5	1	3.5	0.15	1.25	0.1	1.24	1.15	5
Nonlocal lengths	l_{m} (μm)	l_{v} (μm)	l_{d} (μm)						
	40	40	40						

4.3. Validation

4.3.1. Elastoplastic behavior

The numerical simulations are performed with the identified elastoplastic behavior without damage as reported in Fig. 18. The numerical predictions in terms of the engineering stress-strain curves are compared to the corresponding average experimental results. A good agreement before fracture is observed in the cases of the 1L, 2PL, 2NSx, and 3SHEAR specimens as shown in Figs. 18(a)-(c). However, in the case of the grooved plates (7GRx), the numerical predictions overestimate the experimental data as shown in Fig. 18(d). This can be explained by the Lode effect, which is different for this different type of specimens while the elastoplastic constitutive model is not accounting for this effect. A richer plasticity model that includes a Lode effect, *e.g.* $I_1 - J_2 - J_3$ model [58] or Hosford-type model [59], could be used to obtain a better agreement at the low porosities.

4.3.2. Fracture prediction

In this section, the numerical simulations are performed using the nonlocal model (denoted by GTN-Th-Sh) using the identified parameters reported in Tab. 3. Fig. 19 shows the comparison between the numerical predictions with the GTN-Th-Sh model and the corresponding experimental results for all cases. Figs. 19(a, c) show that the model accurately captures the fracture strain of the 1L, 2PL, 3SHEAR specimens and of the 4SR and 5NR4 axisymmetric specimens. However, the GTN-Th-Sh model overestimates the fracture strain of the notched plate (2NSx) specimens as shown in Fig. 19(b). In the cases of the grooved plates (7GRx), the experimental curves prior to the fracture point are overestimated caused by the inaccuracy in the elastoplastic predictions as already reported in Fig. 18. The predicted fracture paths are reported in Appendix B showing a good agreement with the experimental observations.

Figure 20 compares the porosity distribution predicted by the numerical simulations with the experimental measurement described in Section 2.4. The numerical results are consistent with the experimental data.

Figure 21 provides the variations of the stress triaxiality and of the Lode variable at the center of the notched section of each sample as a function of the equivalent plastic deformation. The stress triaxiality is not constant during the loading but varies moderately with plastic deformation. For the cases of 1L, 2PL, 2NS4, 2NS2, 2NS1, the values of the stress triaxiality at the onset of coalescence are very close to each other while the Lode variable significantly differs. In the case of the 3SHEAR sample, a low stress triaxiality is obtained but the Lode variable differs from the pure shear state, *i.e.* $\omega = 0$, and is similar to the 2NS1 sample at the beginning due to the similar notched section geometry. In addition, the fracture does not initiate at the center of the notched section as shown in Fig. 7. The results from the grooved specimens show a steady state of stress triaxiality and Lode parameters except in the case of the 7GR1 sample, in which the stress triaxiality decreases and the Lode parameter increases during the deformation due to the large void
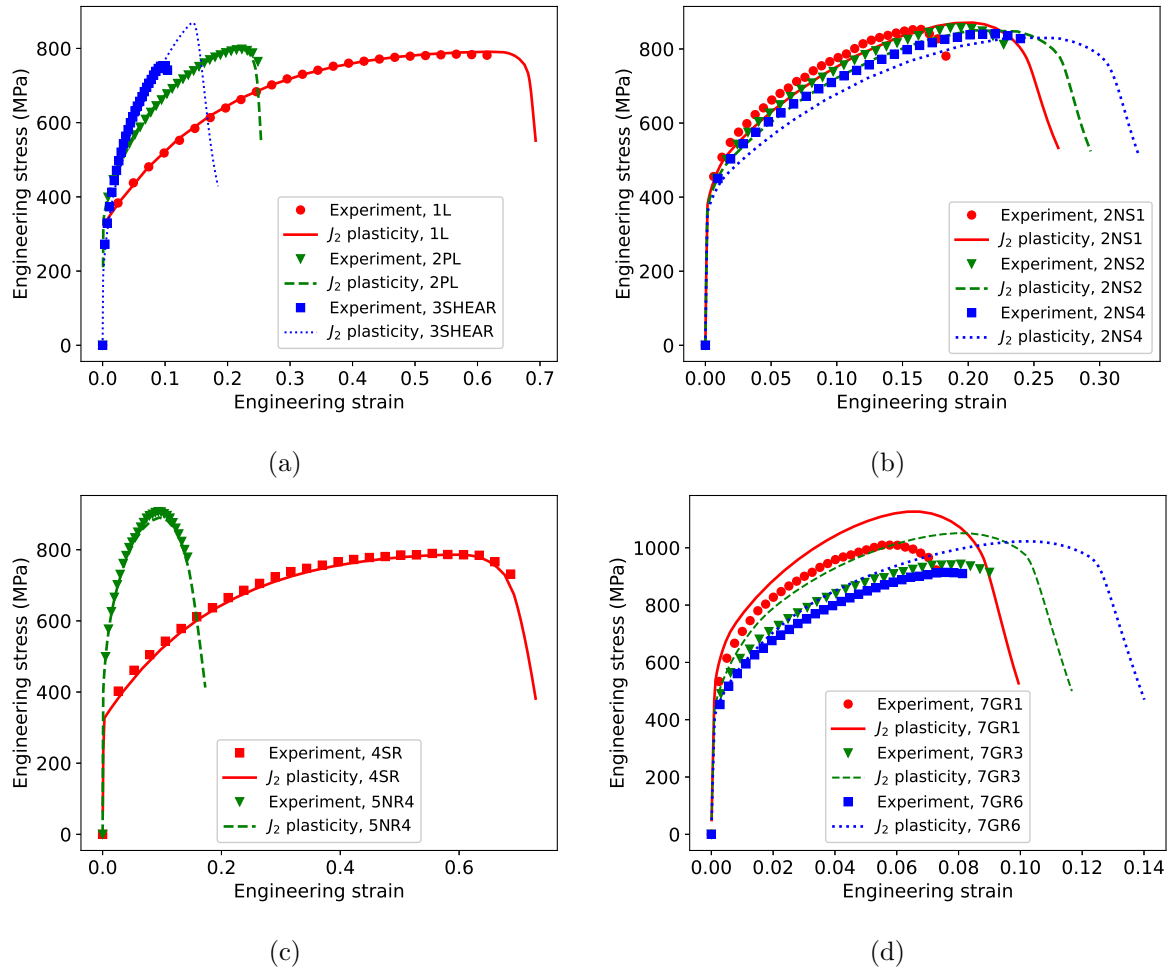
32

(a)

(b)

(c)

(d)

Figure 18: Comparison of the stress-strain responses predicted by the elastoplastic model with the corresponding experimental results for the: (a) smooth (1L), tapered (2PL), and shear (3SHEAR) plates, (b) notched plates (2NS1, 2NS2 and 2NS4), (c) smooth (4SR) and notched (5NR4) round bars, and (d) grooved plates (7GR1, 7GR3 and 7GR6). Only the average responses of the experimental results of Fig. 4 are reported for readability purpose.
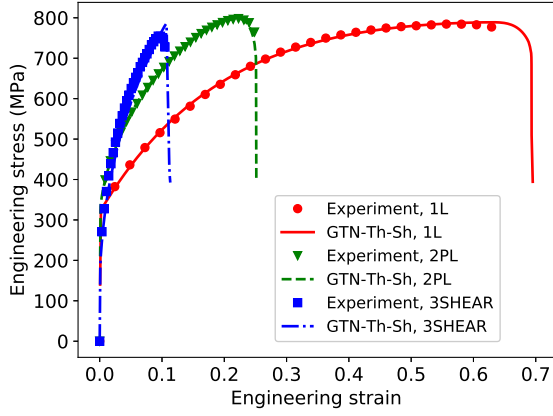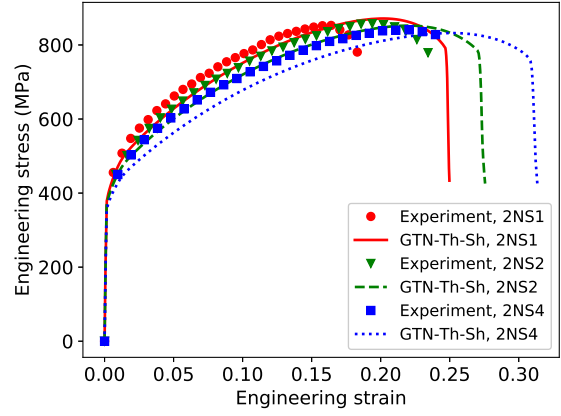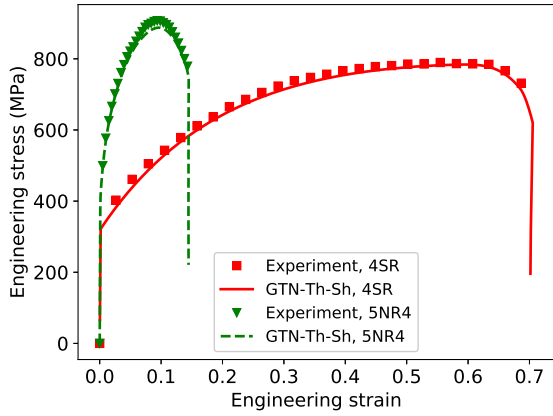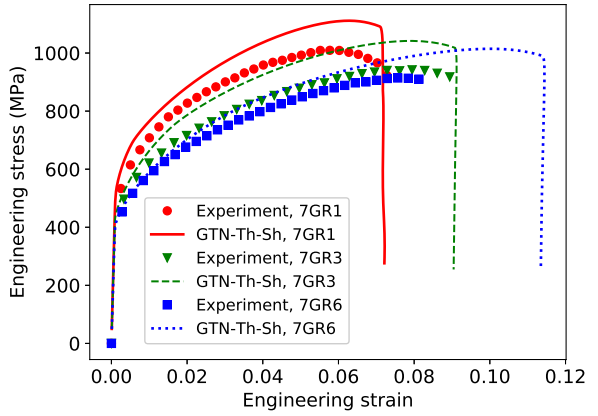
Figure 19: Comparison of the numerical predictions of the multi-yield surface multi-nonlocal variable micromechanics-based ductile failure model with the experimental results for: (a) smooth (1L), tapered (2PL), and shear (3SHEAR) plates, (b) notched plates (2NS1, 2NS2 and 2NS4), (c) smooth (4SR) and notched (5NR4) round bars, and (d) grooved plates (7GR1, 7GR3 and 7GR6). Only the average responses of the experimental results of Fig. 4 are reported for readability purpose.
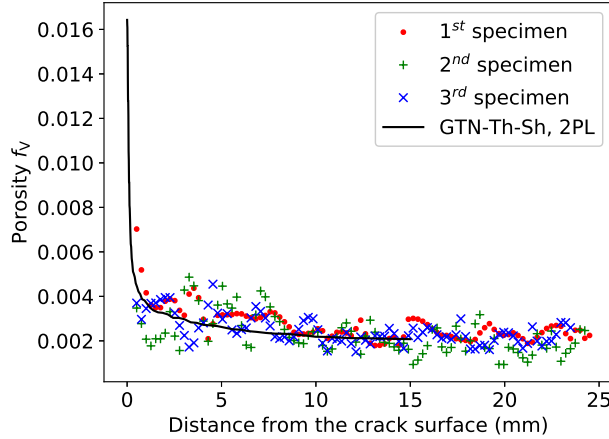
Figure 20: Computed distribution of the porosity distribution in terms of the distance to the fracture surface in the tapered (2PL) specimens. The experimental results reported in Fig. 10 are also reported for comparison purpose.

growth in the high stress triaxiality regime. The largest stress triaxiality at fracture can be obtained with the axisymmetric specimens 4SR and 5NR4 at a constant Lode variable value equal to 1.

Figure 22 shows the distribution of the total displacement field and of $\frac{\partial u_Z}{\partial X}$, where u_Z is the displacement along the loading direction and X is along the width direction, obtained with the current finite element framework and the digital image correlation (DIC) technique for the 3SHEAR specimen. Comparison is made at two engineering strain levels: 0.026 and 0.077. The high strain region at the specimen ligament observed in DIC is accurately captured by numerical simulation.

In Figs. 23, the fracture strain is estimated for each numerical simulation and compared with the corresponding experimental results in terms of the shape factor, stress triaxiality and Lode variable. As repeated before, both the stress triaxiality and the Lode variable affect the fracture strain. Overall, the fraction strain increases with increasing the Lode variable while decreases with increasing stress triaxiality. The numerical simulations provide reasonable predictions of the fracture strain compared to the corresponding experimental data for the different tests.

From an engineering point of view, it is important to define an uncoupled fracture criterion that depends on stress triaxiality η and Lode parameter ω. For this purpose, we follow the fracture criterion proposed in [60] as

$$1 = D = \int_0^{\varepsilon_f} \left[a \exp\left(b\eta\left(\varepsilon_{\mathrm{m}}\right)\right) + c\left(1 - \left| L\left(\varepsilon_{\mathrm{m}}\right)\right|^d\right)\right] d\varepsilon_{\mathrm{m}}\,, \tag{39}$$

where ε_f is the plastic strain at which the fracture starts, η is the stress triaxiality, a, b, c, d are the four constants, L is the other form of the Lode parameter that characterizes the Lode effect, and D is a damage indicator equal to one at fracture. The parameter L relates to the Lode parameter ω used in this work
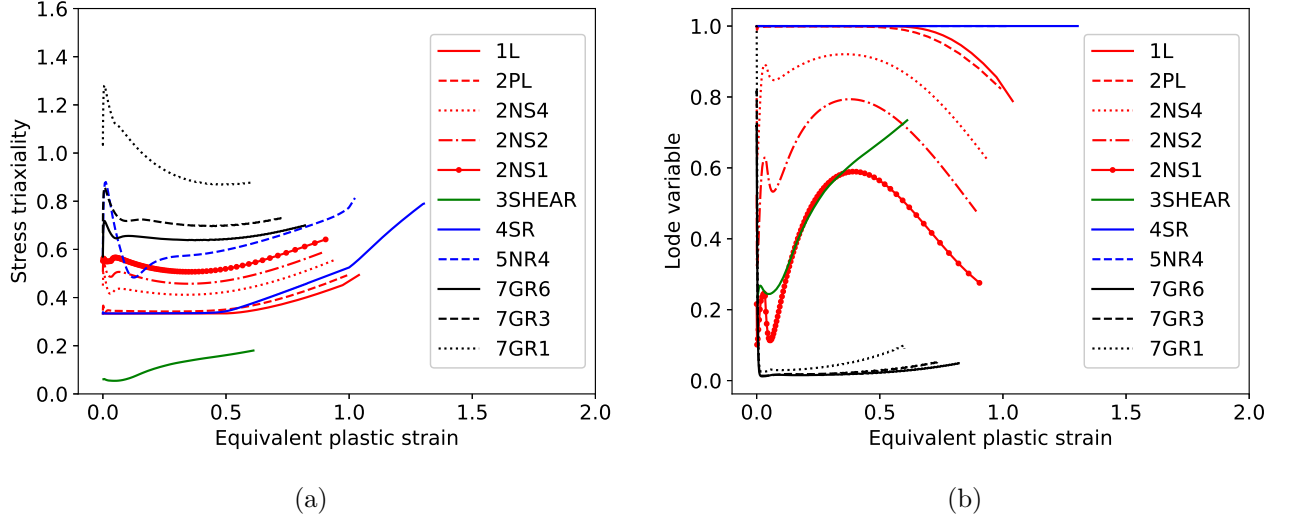
35

(a)

(b)

Figure 21: Variations of the predicted stress triaxiality (a) and Lode variable (b) as a function of the equivalent plastic strain at the center of the notched section for all tests up to the onset of coalescence.

through

$$L = \frac{-3s_2}{s_1 - s_3} = -\sqrt{3}\tan\left(\frac{1}{3}\arccos\omega - \frac{\pi}{6}\right) , \tag{40}$$

where $s_1 \geq s_2 \geq s_3$ are the eigenvalues of the deviatoric stress tensor. Using the curves $\eta\left(\varepsilon_{\mathrm{m}}\right)$ and $\omega\left(\varepsilon_{\mathrm{m}}\right)$ evaluated in Fig. 21, and setting $d = 2$ to compensate the lack of data, the parameters a, b, c of the uncoupled fracture model are identified, yielding

$$a = 0.519\,, b = 1.01\,, c = 0.257\,, \text{ and } d = 2.\,. \tag{41}$$

The identified fracture criterion is visualized in Fig. 24(a) when considering constant triaxiality and Lode parameter, i.e.:

$$\varepsilon_f = \frac{1}{a\exp\left(b\eta\right) + c\left(1 - |L|^d\right)} \,. \tag{42}$$

Figure 24(b) represents the fracture isolines as a function of the stress triaxiality η and the Lode parameter ω evaluated at fracture, i.e. the last points in Fig. 21. The fracture strain increases with an increasing absolute value of the Lode variable while it decreases with an increasing value of the stress triaxiality.

5. Conclusion

In this paper, the fracture behavior of the CoCrNi high entropy alloy is experimentally and numerically investigated under different stress states using flat, axisymmetric, shear, and grooved specimens. A wide range of stress states characterised by the Lode variable and the stress triaxiality was achieved by considering notches of different radius.
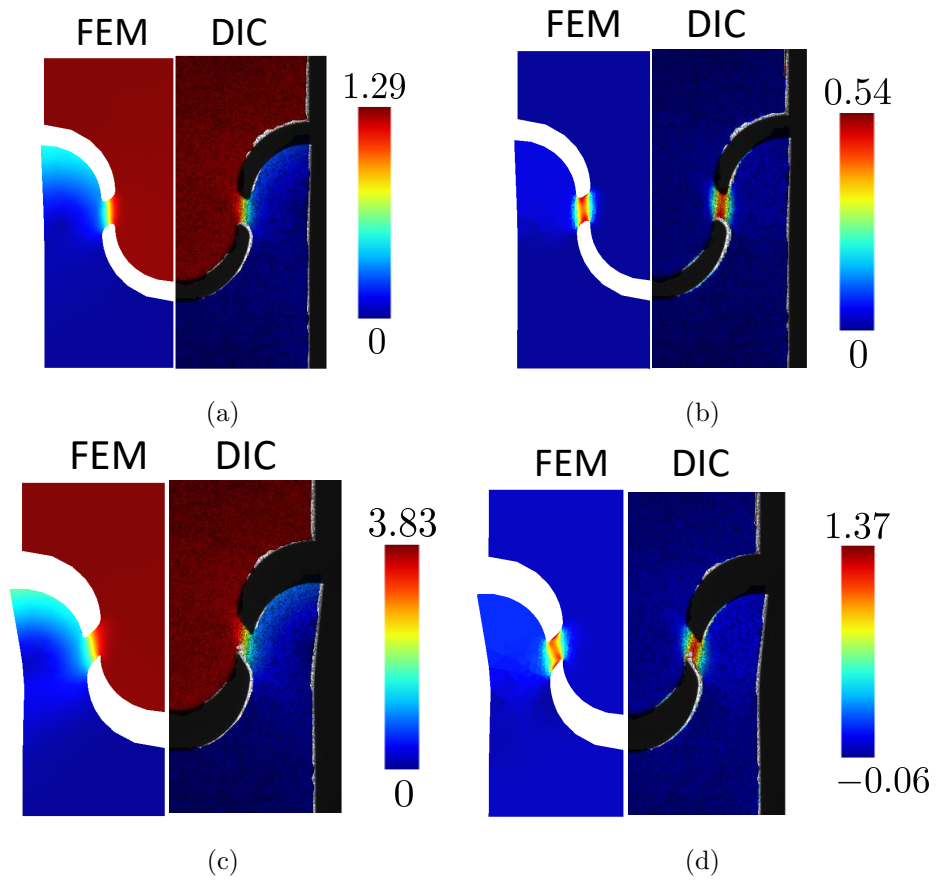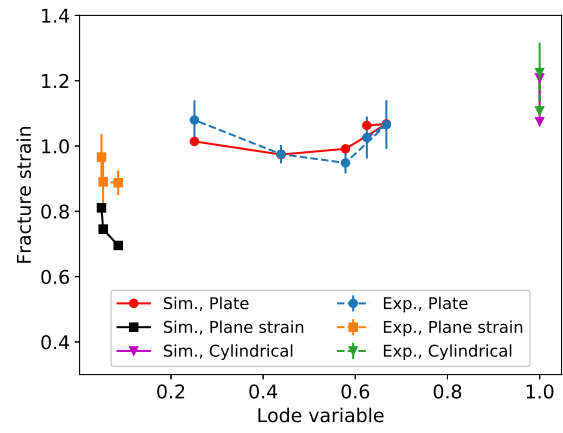
Figure 22: Comparison between the results obtained by the finite element method (FEM) and by the digital image correlation (DIC): (a, b) distributions of, respectively, the total displacement and $\frac{\partial u_Z}{\partial X}$ (u_Z being along the loading direction and X along the sample width direction) at the sample engineering strain equal to 0.026 and (c, d) distributions of, respectively, the total displacement and $\frac{\partial u_Z}{\partial X}$ at the sample engineering strain equal to 0.077.
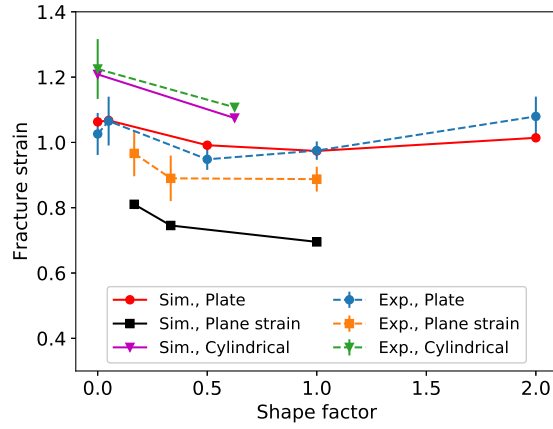
(a)
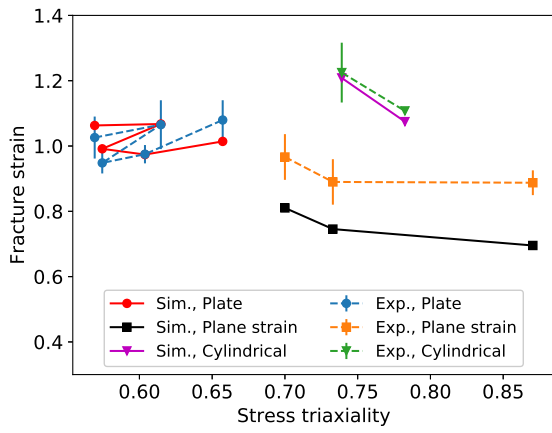
(b)

(c)

Figure 23: Comparison between the fracture strain predicted by the nonlocal GTN-Th-Sh model and the corresponding experimental results in terms of : (a) shape factor and (b, c) respectively the stress triaxiality and Lode variable at the centre of specimen at the onset of the coalescence. The experimental measurements reported in Fig. 5 are reported with their error bars for ease of readability.
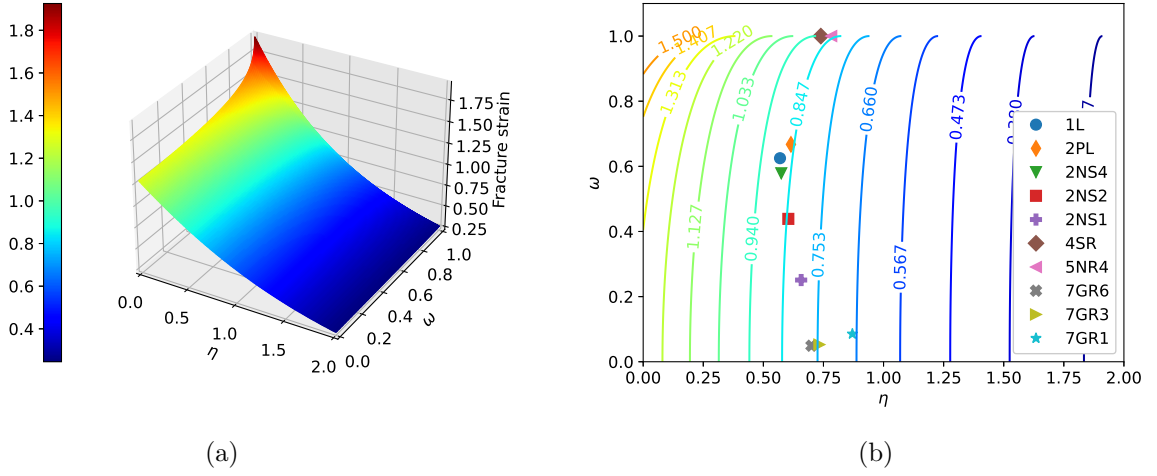
Figure 24: Fracture surface identified for the present material following the uncoupled fracture criterion proposed in [60]: (a) three dimensional view of the fracture surface at constant stress triaxility and Lode parameter and (b) contours of the fracture strain in terms of the stress triaxiality and Lode parameter at fracture in which the different tests are also reported. Only $\omega \geq 0$ is shown because of the symmetry of the fracture surface.

From the experimental study, the following conclusions are drawn:

1. In the CoCrNi alloy under consideration, voids are not initially present. Under loading, the voids nucleate at the early stage of plastic deformation by matrix-inclusion interface decohesion.

2. The stress state strongly affects the fracture behavior. For the plate and grooved specimens, the fracture occurs by the shear-driven coalescence mechanism, leading to a slant fracture surface. For the axisymmetric specimens, the fracture mode first follows the void coalescence by internal necking, then it is driven by the shear coalescence, leading to a cup-cone fracture surface.

3. The CoCrNi alloy is very ductile with a large fracture strain over a wide range of stress states.

The recent multi-yield surface multi-nonlocal variable micromechanics-based ductile failure model developed in [41] is considered to describe the fracture behavior of the CoCrNi alloy. This model allows balancing between micro-mechanics background and computational complexity whilst both internal necking and shear-driven coalescence of voids in a ductile fracture can be modeled. It is shown that the ductile fracture model proposed in [41] captures the fracture behavior of the CoCrNi alloy. After developing an efficient identification procedure of its material parameters, the constitutive model is shown to provide good predictions in terms of stress-strain response, fracture strain, and fracture path over a wide range of stress states. Among others, the flat-slant transition is captured with parameters that were identified without considering that the choice was or not capturing the transition, which is rarely achieved in the context of ductile fracture modeling.
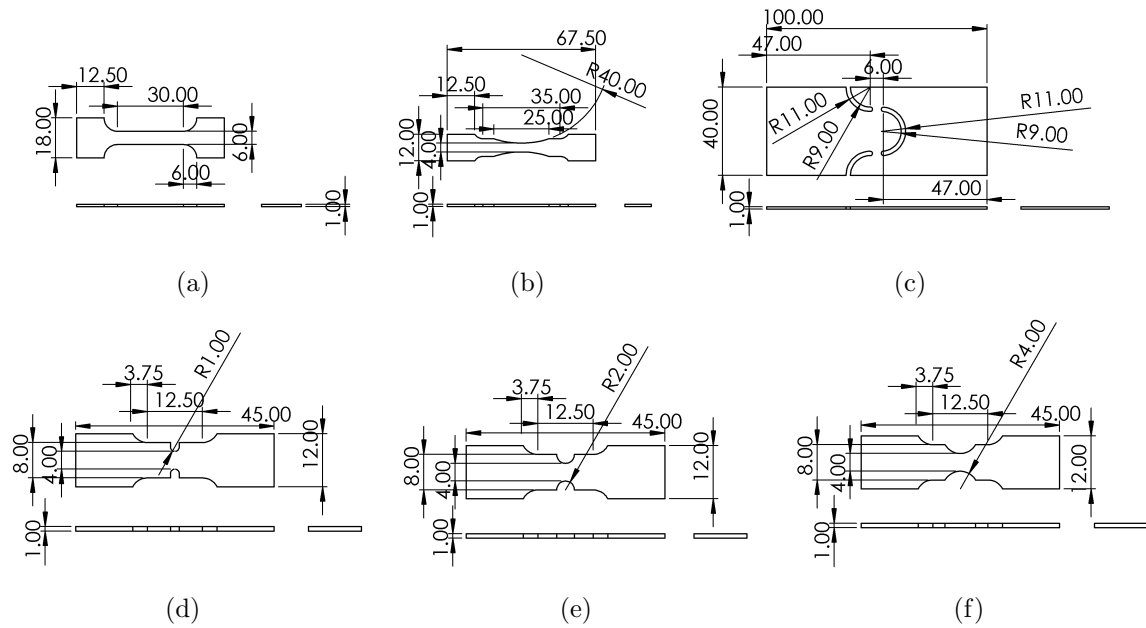
Figure A.25: Geometrical details in mm of the plate specimens: (a) smooth plate (1L), (b) tapered specimen (2PL), (c) shear specimen (3SHEAR), and (d-f) notched specimens (2NS1-2NS4).

As a general conclusion, this study shows that the excellent ductility of HEA Cantor-type alloy has nothing surprising but follows the classical mechanisms of ductile fracture. The low amount of second phase particles, their homogenous distribution, and absence of second population explain the large fracture strain.

Acknowledgments

Data availability

Appendix A. Details of the different sample geometries

The geometrical dimensions the different tested specimens are reported in Figs. A.25-A.27.
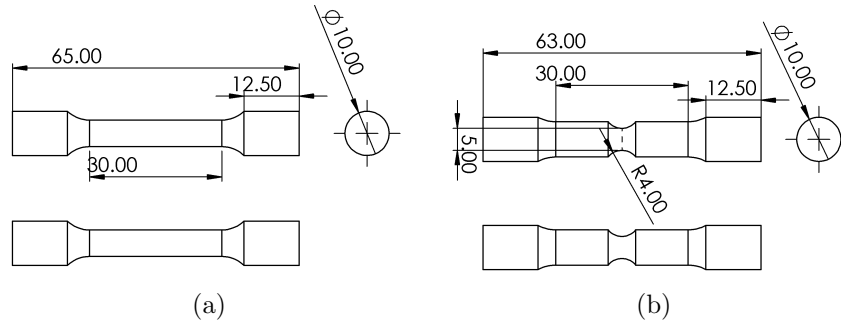
Figure A.26: Geometrical details in mm of the axisymmetric specimens: (a) smooth round bar (4SR), and (b) notched round bar (5NR4).
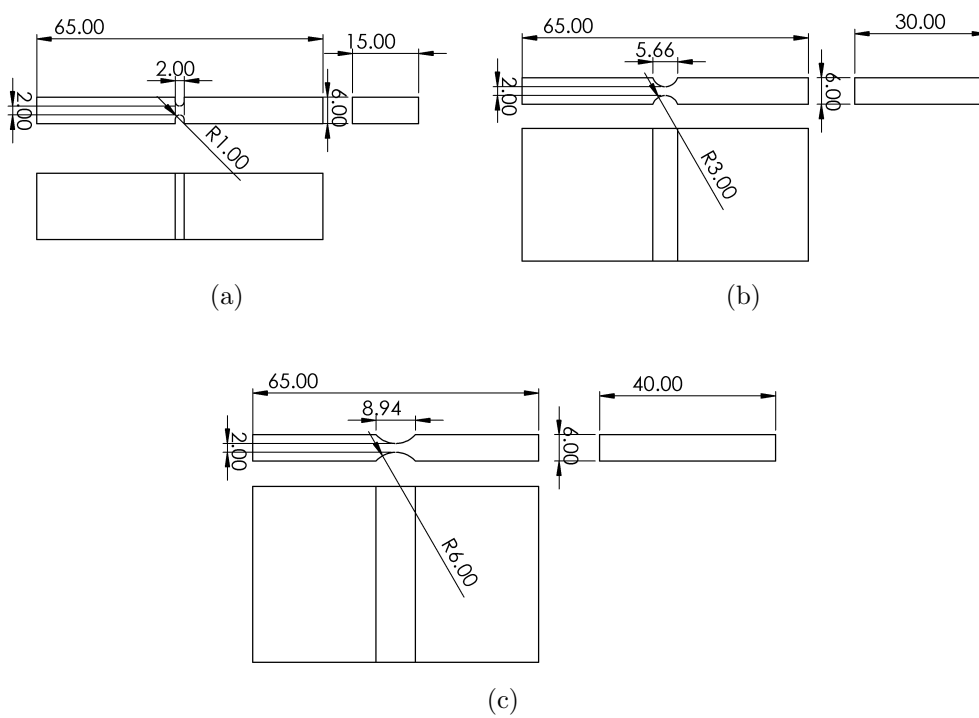
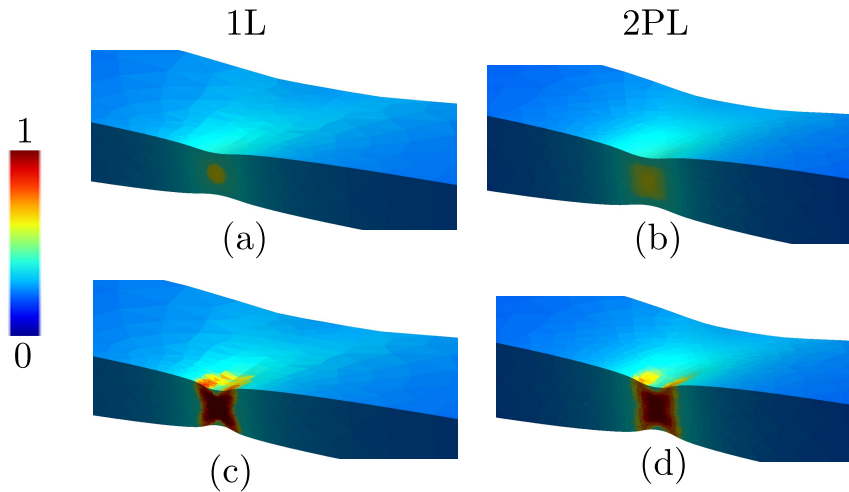Figure A.27: Geometrical details in mm of the grooved plates (7GR1-7GR6).

Figure B.28: Computed distribution of the void ligament ratio in the smooth (1L) and tapered (2PL) plates: (a, b) at the onset of coalescence and (c, d) at the fracture. The shear-driven coalescence is the fracture mechanism observed and predicted for these tests.

Appendix B. Fracture path

The fracture mode for the plate specimens is experimentally to be by a void shearing coalescence mechanism. This behavior is captured by the multi-yield surface multi-nonlocal variable micromechanics-based ductile failure model as shown by Figs. B.28-B.29 for the smooth (1L) and tapered (2PL) plates, and by Figs. B.30-B.31 for the notched plates (2PL, and 2NS1, 2NS2). Indeed, the distributions of the void ligament ratio of these specimens, see Figs. B.28 and B.30, agree with the experimental slant fracture path, see Figs. 9. Since constant nonlocal length scales are employed, the damage (here represented by the ligament ratio) undergoes a widening effect and the slant paths in the 1L, 2PL, and 2NS1, 2NS2, and 2NS4 specimens are more visible in the distribution of the mean equivalent plastic strain of the matrix reported in Figs. B.29, B.31. Fig. B.32 shows the distribution of the void ligament ratio of the 3SHEAR specimen at the onset of the coalescence and at the end of the numerical simulation. It is found that the fracture path agrees well with the experimental observation reported in Fig. 7(b).

For the axisymmetric specimens, the distribution of the void ligament ratio along a transverse middle cross section is shown in Fig. B.33 at the onset of coalescence and at the final fracture stage. The fracture process is driven by internal necking of voids at the centre of the specimen and by the void shearing coalescence near free boundaries. The predicted fracture path follows a cup-cone shape, which agrees with the experimental observations reported Fig. 6.

In the cases of the grooved plates (7GRx), the distribution of the void ligament ratio is shown in Fig. B.34. The fracture process is driven by the void shearing coalescence mode. The slant fracture mode is observed for those tests, which agrees well with the experimental observations reported in Fig. 8.
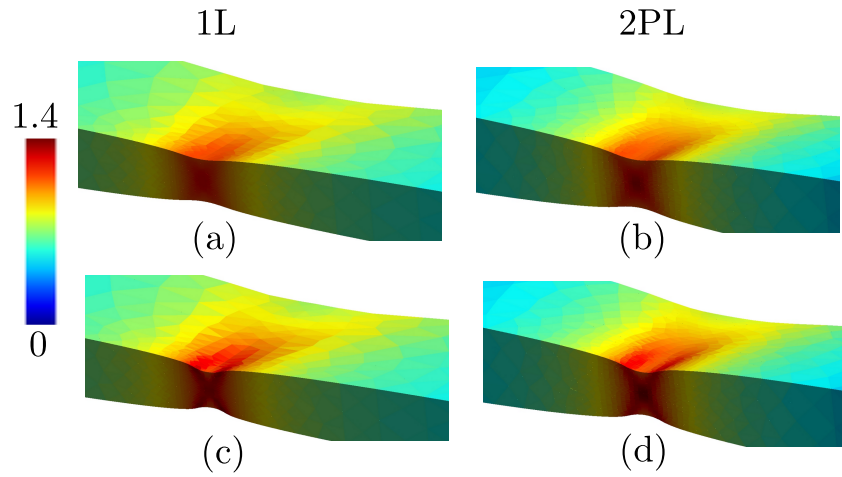
Figure B.29: Computed distribution of the equivalent plastic deformation in the matrix in the smooth (1L) and tapered (2PL) plates: (a, b) at the onset of coalescence and (c, d) at the fracture. The shear-driven coalescence is the fracture mechanism observed and predicted for these tests.
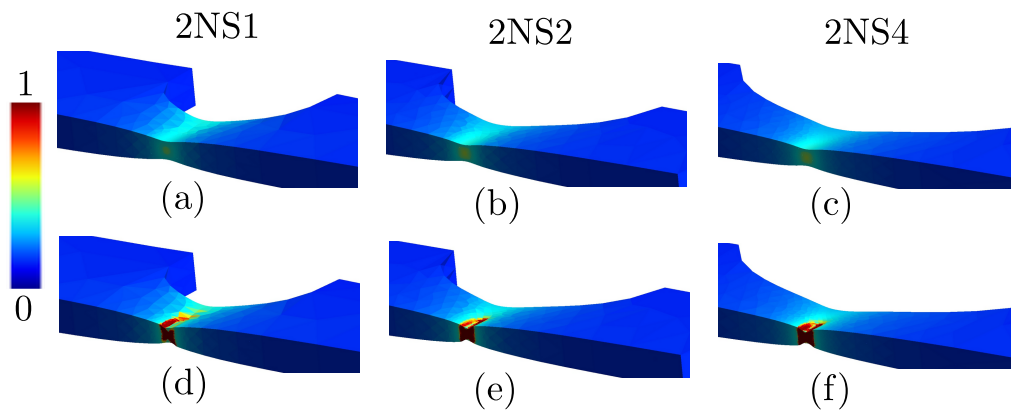

Figure B.30: Computed distribution of the void ligament ratio in 2NSx tests: (a, b, c) at the onset of coalescence and (d, e, f) at the fracture. The shear-driven coalescence is the fracture mechanism observed and predicted for these tests.
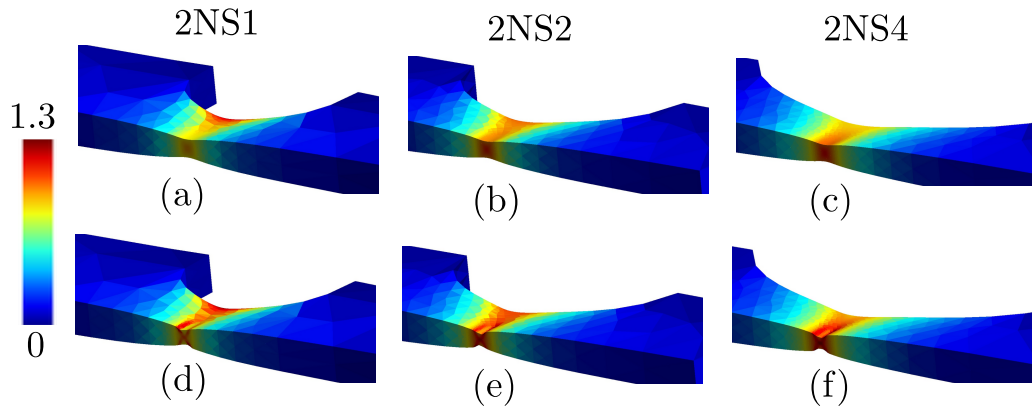
Figure B.31: Computed distribution of the equivalent plastic deformation in the matrix in notched plates (2NSx): (a, b, c) at the onset of coalescence and (d, e, f) at the fracture. The shear-driven coalescence is the fracture mechanism observed and predicted for these tests.
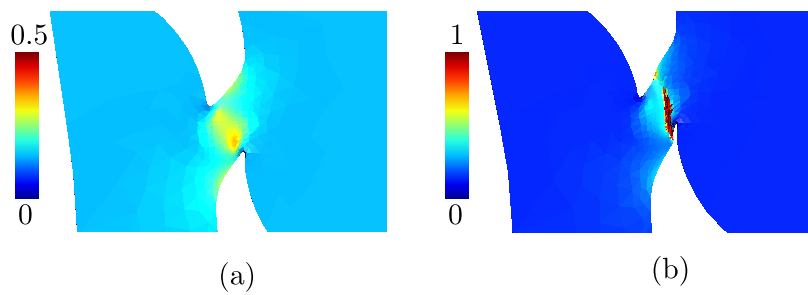

Figure B.32: Computed distribution of the void ligament ratio in the shear plate (3SHEAR): (a) at the onset of coalescence and (b) at the fracture. The shear-driven coalescence is the fracture mechanism observed and predicted for this test.
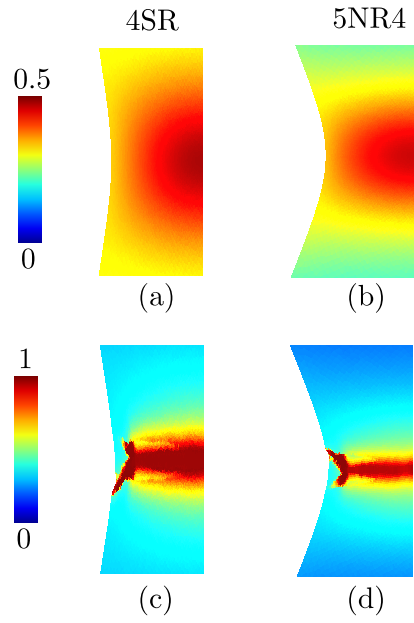
Figure B.33: Computed distribution of the void ligament ratio χ in the smooth (4SR) and notched (5NR4) round specimens: (a, b) at the onset of coalescence and (c, d) at the fracture. Cup-cone fracture profiles are observed and predicted.
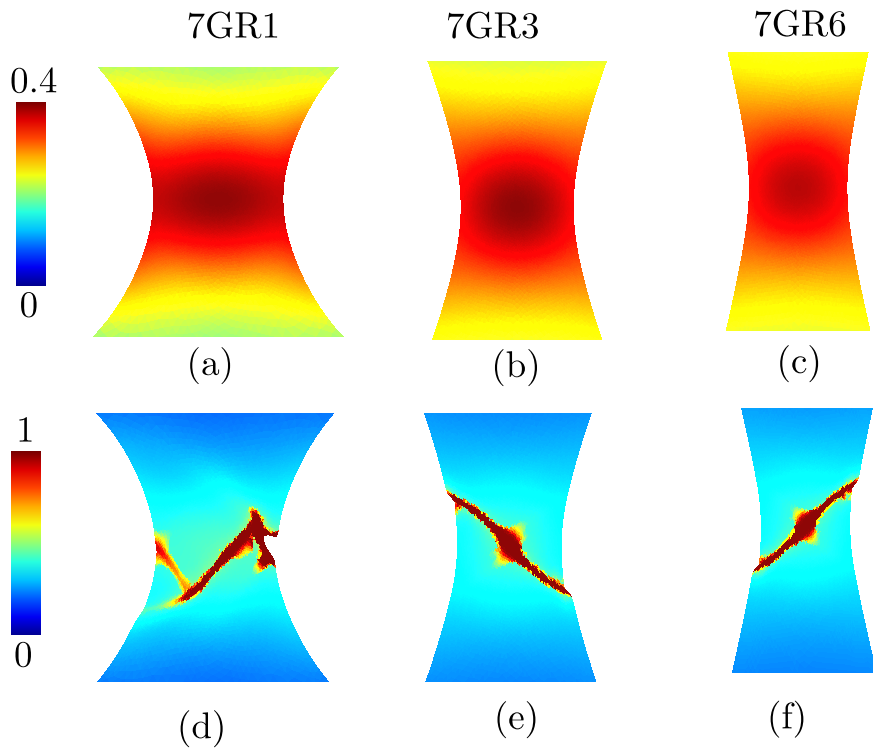

Figure B.34: Computed distribution of the void ligament ratio χ in the grooved specimens (7GRx): (a, b) at the onset of coalescence and (c, d) at the fracture. Slant fracture mode by shear-driven mechanism is observed and predicted.

References

[1] D. B. Miracle, O. N. Senkov, A critical review of high entropy alloys and related concepts, Acta Materialia 122 (2017) 448–511 (2017).

[2] W. Li, D. Xie, D. Li, Y. Zhang, Y. Gao, P. K. Liaw, Mechanical behavior of high-entropy alloys, Progress in Materials Science 118 (2021) 100777 (2021). `doi:https://doi.org/10.1016/j.pmatsci.2021.100777`.
URL `https://www.sciencedirect.com/science/article/pii/S0079642521000013`

[3] E. P. George, W. Curtin, C. C. Tasan, High entropy alloys: A focused review of mechanical properties and deformation mechanisms, Acta Materialia 188 (2020) 435–474 (2020).

[4] Z. Wu, H. Bei, G. M. Pharr, E. P. George, Temperature dependence of the mechanical properties of equiatomic solid solution alloys with face-centered cubic crystal structures, Acta Materialia 81 (2014) 428–441 (2014).

[5] B. Gludovatz, A. Hohenwarter, D. Catoor, E. H. Chang, E. P. George, R. O. Ritchie, A fracture-resistant high-entropy alloy for cryogenic applications, Science 345 (6201) (2014) 1153–1158 (2014).

[6] B. Gludovatz, A. Hohenwarter, K. V. Thurston, H. Bei, Z. Wu, E. P. George, R. O. Ritchie, Exceptional damage-tolerance of a medium-entropy alloy crconi at cryogenic temperatures, Nature communications 7 (2016) 10602 (2016).

[7] G. Laplanche, A. Kostka, O. Horst, G. Eggeler, E. George, Microstructure evolution and critical stress for twinning in the crmnfeconi high-entropy alloy, Acta Materialia 118 (2016) 152–163 (2016).

[8] G. Laplanche, A. Kostka, C. Reinhart, J. Hunfeld, G. Eggeler, E. George, Reasons for the superior mechanical properties of medium-entropy crconi compared to high-entropy crmnfeconi, Acta Materialia 128 (2017) 292–303 (2017).

[9] O. Bouaziz, J. Moon, H. S. Kim, Y. Estrin, Isotropic and kinematic hardening of a high entropy alloy, Scripta Materialia 191 (2021) 107–110 (2021).

[10] Y. Kim, H. K. Park, P. Asghari-Rad, J. Jung, J. Moon, H. S. Kim, Constitutive modeling with critical twinning stress in cocrfemnni high entropy alloy at cryogenic temperature and room temperature, Metals and Materials International 27 (7) (2021) 2300–2309 (2021).

[11] X. Liu, H. Feng, J. Wang, X. Chen, P. Jiang, F. Yuan, H. Li, E. Ma, X. Wu, Mechanical property comparisons between crconi medium-entropy alloy and 316 stainless steels, Journal of Materials Science & Technology 108 (2022) 256–269 (2022).

[12] M. Yang, L. Zhou, C. Wang, P. Jiang, F. Yuan, E. Ma, X. Wu, High impact toughness of crconi medium-entropy alloy at liquid-helium temperature, Scripta Materialia 172 (2019) 66–71 (2019).

[13] B. Gao, G. Zhang, T. Guo, C. Jiang, X. Guo, S. Tang, Voiding and fracture in high-entropy alloy under multi-axis stress states, Materials Letters 237 (2019) 220–223 (2019).

[14] P. Lu, T. Zhang, D. Zhao, S. Ma, Q. Li, T. Wang, Z. Wang, Effects of stress states and strain rates on mechanical behavior and texture evolution of the cocrfeni high-entropy alloy: experiment and simulation, Journal of Alloys and Compounds 851 (2021) 156779 (2021).

[15] Y. Cui, Z. Chen, Y. Ju, Fracture of void-embedded high-entropy-alloy films: A comprehensive atomistic study, Materialia 12 (2020) 100790 (2020).

[16] T. Pardoen, F. Scheyvaerts, A. Simar, C. Tekoglu, P. R. Onck, Multiscale modeling of ductile failure in metallic alloys, Comptes Rendus Physique 11 (3) (2010) 326–345, computational metallurgy and scale transitions (2010). `doi:https://doi.org/10.1016/j.crhy.2010.07.012`.
URL `https://www.sciencedirect.com/science/article/pii/S1631070510000770`

[17] A. A. Benzerga, J.-B. Leblond, A. Needleman, V. Tvergaard, Ductile failure modeling, International Journal of Fracture 201 (1) (2016) 29–80 (Sep 2016). `doi:10.1007/s10704-016-0142-6`.
URL `https://doi.org/10.1007/s10704-016-0142-6`

[18] A. Pineau, A. Benzerga, T. Pardoen, Failure of metals i: Brittle and ductile fracture, Acta Materialia 107 (2016) 424 –

483 (2016). doi:https://doi.org/10.1016/j.actamat.2015.12.034.

URL http://www.sciencedirect.com/science/article/pii/S1359645415301403

[19] A. Pineau, T. Pardoen, Failure mechanisms of metals, Comprehensive structural integrity encyclopedia 2 (2007) 687–783 (2007).

[20] A. L. Gurson, Continuum theory of ductile rupture by void nucleation and growth: Part i - yield criteria and flow rules for porous ductile media, Journal of Engineering Materials and Technology 99 (1) (1977) 2–15 (1977).

[21] V. Tvergaard, A. Needleman, Analysis of the cup-cone fracture in a round tensile bar, Acta Metallurgica 32 (1) (1984) 157 − 169 (1984). doi:https://doi.org/10.1016/0001-6160(84)90213-X.

URL http://www.sciencedirect.com/science/article/pii/000161608490213X

[22] A. Needleman, V. Tvergaard, An analysis of ductile rupture in notched bars, Journal of the Mechanics and Physics of Solids 32 (6) (1984) 461 − 490 (1984). doi:https://doi.org/10.1016/0022-5096(84)90031-0.

URL http://www.sciencedirect.com/science/article/pii/0022509684900310

[23] C. Chu, A. Needleman, Void nucleation effects in biaxially stretched sheets, Journal of engineering materials and technology 102 (3) (1980) 249–256 (1980).

[24] M. Gologanu, J.-B. Leblond, J. Devaux, Approximate models for ductile metals containing nonspherical voids - case of axisymmetric oblate ellipsoidal cavities, Journal of Engineering Materials and Technology 116 (3) (1994) 290–297 (1994).

[25] M. Gologanu, J.-B. Leblond, J. Devaux, Approximate models for ductile metals containing non-spherical voids - case of axisymmetric prolate ellipsoidal cavities, Journal of the Mechanics and Physics of Solids 41 (11) (1993) 1723 − 1754 (1993). doi:https://doi.org/10.1016/0022-5096(93)90029-F.

URL http://www.sciencedirect.com/science/article/pii/002250969390029F

[26] S. Keralavarma, A. Benzerga, A constitutive model for plastically anisotropic solids with non-spherical voids, Journal of the Mechanics and Physics of Solids 58 (6) (2010) 874 − 901 (2010). doi:https://doi.org/10.1016/j.jmps.2010.03.007.

URL http://www.sciencedirect.com/science/article/pii/S0022509610000682

[27] F. Scheyvaerts, P. Onck, C. Tekoğlu, T. Pardoen, The growth and coalescence of ellipsoidal voids in plane strain under combined shear and tension, Journal of the Mechanics and Physics of Solids 59 (2) (2011) 373 − 397 (2011). doi:https://doi.org/10.1016/j.jmps.2010.10.003.

URL http://www.sciencedirect.com/science/article/pii/S0022509610002061

[28] A. Benzerga, J. Besson, A. Pineau, Anisotropic ductile fracture: Part ii: theory, Acta Materialia 52 (15) (2004) 4639 − 4650 (2004). doi:https://doi.org/10.1016/j.actamat.2004.06.019.

URL http://www.sciencedirect.com/science/article/pii/S135964540400357X

[29] C. Felipe Guzmn, E. I. Saavedra Flores, A. M. Habraken, Damage characterization in a ferritic steel sheet: Experimental tests, parameter identification and numerical modeling, International Journal of Solids and Structures 155 (2018) 109 − 122 (2018). doi:https://doi.org/10.1016/j.ijsolstr.2018.07.014.

URL http://www.sciencedirect.com/science/article/pii/S002076831830297X

[30] K. Nahshon, J. Hutchinson, Modification of the gurson model for shear failure, European Journal of Mechanics - A/Solids 27 (1) (2008) 1 − 17 (2008). doi:https://doi.org/10.1016/j.euromechsol.2007.08.002.

URL http://www.sciencedirect.com/science/article/pii/S0997753807000721

[31] L. Xue, Constitutive modeling of void shearing effect in ductile fracture of porous materials, Engineering Fracture Mechanics 75 (11) (2008) 3343 − 3366, local Approach to Fracture (19862006): Selected papers from the 9th European Mechanics of Materials Conference (2008). doi:https://doi.org/10.1016/j.engfracmech.2007.07.022.

URL http://www.sciencedirect.com/science/article/pii/S0013794407003220

[32] T. Pardoen, J. Hutchinson, An extended model for void growth and coalescence, Journal of the Mechanics and Physics of Solids 48 (12) (2000) 2467 − 2512 (2000). doi:https://doi.org/10.1016/S0022-5096(00)00019-3.

URL `http://www.sciencedirect.com/science/article/pii/S0022509600000193`

[33] J. Koplik, A. Needleman, Void growth and coalescence in porous plastic solids, International Journal of Solids and Structures 24 (8) (1988) 835 – 853 (1988). `doi:https://doi.org/10.1016/0020-7683(88)90051-0`.
URL `http://www.sciencedirect.com/science/article/pii/0020768388900510`

[34] P. Thomason, A three-dimensional model for ductile fracture by the growth and coalescence of microvoids, Acta Metallurgica 33 (6) (1985) 1087 – 1095 (1985). `doi:https://doi.org/10.1016/0001-6160(85)90202-0`.
URL `http://www.sciencedirect.com/science/article/pii/0001616085902020`

[35] P. Thomason, Three-dimensional models for the plastic limit-loads at incipient failure of the intervoid matrix in ductile porous solids, Acta Metallurgica 33 (6) (1985) 1079 – 1085 (1985). `doi:https://doi.org/10.1016/0001-6160(85)90201-9`.
URL `http://www.sciencedirect.com/science/article/pii/0001616085902019`

[36] A. Benzerga, Micromechanics of coalescence in ductile fracture, Journal of the Mechanics and Physics of Solids 50 (6) (2002) 1331 – 1362 (2002). `doi:https://doi.org/10.1016/S0022-5096(01)00125-9`.
URL `http://www.sciencedirect.com/science/article/pii/S0022509601001259`

[37] F. Scheyvaerts, T. Pardoen, P. Onck, A new model for void coalescence by internal necking, International Journal of Damage Mechanics 19 (1) (2010) 95–126 (2010). `arXiv:https://doi.org/10.1177/1056789508101918`, `doi:10.1177/1056789508101918`.
URL `https://doi.org/10.1177/1056789508101918`

[38] A. A. Benzerga, J.-B. Leblond, Effective yield criterion accounting for microvoid coalescence, Journal of Applied Mechanics 81 (3) (2014) 031009 (2014).

[39] C. Tekoğlu, J.-B. Leblond, T. Pardoen, A criterion for the onset of void coalescence under combined tension and shear, Journal of the Mechanics and Physics of Solids 60 (7) (2012) 1363 – 1381 (2012). `doi:https://doi.org/10.1016/j.jmps.2012.02.006`.
URL `http://www.sciencedirect.com/science/article/pii/S0022509612000373`

[40] M. E. Torki, A unified criterion for void growth and coalescence under combined tension and shear, International Journal of Plasticity 119 (2019) 57 – 84 (2019). `doi:https://doi.org/10.1016/j.ijplas.2019.02.002`.
URL `http://www.sciencedirect.com/science/article/pii/S0749641918303152`

[41] V.-D. Nguyen, T. Pardoen, L. Noels, A nonlocal approach of ductile failure incorporating void growth, internal necking, and shear dominated coalescence mechanisms, Journal of the Mechanics and Physics of Solids 137 (2020) 103891 (2020). `doi:https://doi.org/10.1016/j.jmps.2020.103891`.
URL `https://www.sciencedirect.com/science/article/pii/S0022509619309275`

[42] M. G. D. Geers, R. H. J. Peerlings, W. A. M. Brekelmans, R. de Borst, Phenomenological nonlocal approaches based on implicit gradient-enhanced damage, Acta Mechanica 144 (1) (2000) 1–15 (Mar 2000). `doi:10.1007/BF01181824`.
URL `https://doi.org/10.1007/BF01181824`

[43] R. Peerlings, M. Geers, R. de Borst, W. Brekelmans, A critical comparison of nonlocal and gradient-enhanced softening continua, International Journal of Solids and Structures 38 (44) (2001) 7723 – 7746 (2001). `doi:https://doi.org/10.1016/S0020-7683(01)00087-7`.
URL `http://www.sciencedirect.com/science/article/pii/S0020768301000877`

[44] Y. Liu, L. Kang, H. Ge, Experimental and numerical study on ductile fracture of structural steels under different stress states, Journal of Constructional Steel Research 158 (2019) 381–404 (2019). `doi:https://doi.org/10.1016/j.jcsr.2019.04.001`.
URL `https://www.sciencedirect.com/science/article/pii/S0143974X18313439`

[45] Y. Bai, T. Wierzbicki, A new model of metal plasticity and fracture with pressure and lode dependence, International Journal of Plasticity 24 (6) (2008) 1071 – 1096 (2008). `doi:https://doi.org/10.1016/j.ijplas.2007.09.004`.

URL `http://www.sciencedirect.com/science/article/pii/S0749641907001246`

[46] M. Marteleur, J. Leclerc, M.-S. Colla, V.-D. Nguyen, L. Noels, T. Pardoen, Ductile fracture of high strength steels with morphological anisotropy, part i: Characterization, testing, and void nucleation law, Engineering Fracture Mechanics 244 (2021) 107569 (2021). `doi:https://doi.org/10.1016/j.engfracmech.2021.107569`.
URL `https://www.sciencedirect.com/science/article/pii/S0013794421000424`

[47] F. Hannard, T. Pardoen, E. Maire, C. Le Bourlot, R. Mokso, A. Simar, Characterization and micromechanical modelling of microstructural heterogeneity effects on ductile fracture of 6xxx aluminium alloys, Acta Materialia 103 (2016) 558–572 (2016). `doi:10.1016/j.actamat.2015.10.008`.
URL `https://linkinghub.elsevier.com/retrieve/pii/S1359645415300094`

[48] L. Lecarme, E. Maire, A. Kumar K.C., C. De Vleeschouwer, L. Jacques, A. Simar, T. Pardoen, Heterogenous void growth revealed by in situ 3-d x-ray microtomography using automatic cavity tracking, Acta Materialia 63 (2014) 130–139 (2014). `doi:https://doi.org/10.1016/j.actamat.2013.10.014`.
URL `https://www.sciencedirect.com/science/article/pii/S1359645413007659`

[49] Z. Wu, Y. Gao, H. Bei, Thermal activation mechanisms and labusch-type strengthening analysis for a family of high-entropy and equiatomic solid-solution alloys, Acta Materialia 120 (2016) 108–119 (2016). `doi:https://doi.org/10.1016/j.actamat.2016.08.047`.
URL `https://www.sciencedirect.com/science/article/pii/S1359645416306255`

[50] B. Guan, Y. Wang, J. Li, Y. Zhang, H. Wang, Y. Xin, Comprehensive study of strain hardening behavior of crconi medium-entropy alloy, Journal of Alloys and Compounds 882 (2021) 160623 (2021).

[51] R. H. J. Peerlings, R. De Borst, W. A. M. Brekelmans, J. H. P. De Vree, Gradient enhanced damage for quasi-brittle materials, International Journal for Numerical Methods in Engineering 39 (19) (1996) 3391–3403 (1996).
URL `http://www.scopus.com/inward/record.url?eid=2-s2.0-0030267284&partnerID=tZOtx3y1`

[52] A. A. Benzerga, J.-B. Leblond, Ductile fracture by void growth to coalescence, in: H. Aref, E. van der Giessen (Eds.), Advances in Applied Mechanics, Vol. 44 of Advances in Applied Mechanics, Elsevier, 2010, pp. 169 – 305 (2010). `doi:https://doi.org/10.1016/S0065-2156(10)44003-X`.
URL `http://www.sciencedirect.com/science/article/pii/S006521561044003X`

[53] V. Tvergaard, Effect of stress-state and spacing on voids in a shear-field, International Journal of Solids and Structures 49 (22) (2012) 3047–3054 (2012). `doi:https://doi.org/10.1016/j.ijsolstr.2012.06.008`.
URL `https://www.sciencedirect.com/science/article/pii/S0020768312002636`

[54] V. Tvergaard, On localization in ductile materials containing spherical voids, International Journal of fracture 18 (4) (1982) 237–252 (1982).

[55] K. L. Nielsen, V. Tvergaard, Ductile shear failure or plug failure of spot welds modelled by modified gurson model, Engineering Fracture Mechanics 77 (7) (2010) 1031 – 1047 (2010). `doi:https://doi.org/10.1016/j.engfracmech.2010.02.031`.
URL `http://www.sciencedirect.com/science/article/pii/S0013794410001128`

[56] M. G. Geers, R. De Borst, W. A. Brekelmans, R. H. Peerlings, Strain-based transient-gradient damage model for failure analyses, Computer Methods in Applied Mechanics and Engineering 160 (1-2) (1998) 133–153 (1998). `doi:10.1016/S0045-7825(98)80011-X`.
URL `http://www.sciencedirect.com/science/article/pii/S004578259880011X`

[57] A. E. O. Tuhami, S. Feld-Payet, S. Quilici, N. Osipov, J. Besson, A two characteristic length nonlocal gtn model: Application to cupcone and slant fracture, Mechanics of Materials 171 (2022) 104350 (2022). `doi:https://doi.org/10.1016/j.mechmat.2022.104350`.
URL `https://www.sciencedirect.com/science/article/pii/S0167663622001272`

[58] X. Gao, T. Zhang, J. Zhou, S. M. Graham, M. Hayden, C. Roe, On stress-state dependent plasticity modeling: Significance of the hydrostatic stress, the third invariant of stress deviator and the non-associated flow rule, International Journal of Plasticity 27 (2) (2011) 217–231 (2011). `doi:10.1016/j.ijplas.2010.05.004`.
URL `http://dx.doi.org/10.1016/j.ijplas.2010.05.004`

[59] W. F. Hosford, A Generalized Isotropic Yield Criterion, Journal of Applied Mechanics 39 (2) (1972) 607–609 (06 1972). `doi:10.1115/1.3422732`.
URL `https://doi.org/10.1115/1.3422732`

[60] C. Defaisse, M. Mazire, L. Marcin, J. Besson, Ductile fracture of an ultra-high strength steel under low to moderate stress triaxiality, Engineering Fracture Mechanics 194 (2018) 301–318 (2018). `doi:https://doi.org/10.1016/j.engfracmech.2017.12.035`.
URL `https://www.sciencedirect.com/science/article/pii/S0013794417310147`

[61] A. Hilhorst, J. Leclerc, T. Pardoen, P. J. Jacques, L. Noels, V.-D. Nguyen, Data of "Ductile fracture of high entropy alloys: from the design of an experimental campaign to the development of a micromechanics-based modeling framework", The research has been funded by the Walloon Region under the agreement no. 1610154-EntroTough in the context of the 2016 WalInnov call. (2022). `doi:10.5281/zenodo.7093549`.
URL `https://doi.org/10.5281/zenodo.7093549`